NAIST-IS-DD1161022

Doctoral Dissertation

Bayesian Cell Force Estimation Considering Force Directions

Satoshi Kozawa

June 2, 2014

Department of Information Science
Graduate School of Information Science
Nara Institute of Science and Technology

A Doctoral Dissertation
submitted to Graduate School of Information Science,
Nara Institute of Science and Technology
in partial fulfillment of the requirements for the degree of
Doctor of ENGINEERING

Satoshi Kozawa

Thesis Committee:

Professor Kazushi Ikeda	(Supervisor)
Professor Shigehiko Kanaya	(Co-supervisor)
Associate Professor Tadao Sugiura	(Co-supervisor)
Associate Professor Yuichi Sakumura	(Aichi Prefectural University)
Associate Professor Naoyuki Inagaki	(Graduate School of Biological Sciences)

Bayesian Cell Force Estimation Considering Force Directions*

Satoshi Kozawa

Abstract

Traction force microscopy is a useful technique for measuring mechanical forces generated by cells. In this method, fluorescent nano beads are embedded in the elastic substrate in cell culture, on which cells are cultured. Then, cellular forces are estimated from bead displacements, which represent the force-induced deformation of the substrate under the cell. Estimating the forces from the bead displacements is not easy when the bead density is low or the locations of cellular attachments are unknown. In this study, I propose a Bayesian algorithm by introducing a prior force direction that is based on cellular morphology. I apply the Bayesian framework to synthetic and real datasets in conditions under which the bead density is low and cellular attachment points are unknown. We demonstrate that the Bayesian algorithm improves accuracy in force estimation compared with the previous algorithms.

Keywords:

Bayes inference, Variational-Bayes Approximation, EM algorithm, Traction force microscopy

*Doctoral Dissertation, Department of Information Science, Graduate School of Information Science, Nara Institute of Science and Technology, NAIST-IS-DD1161022, June 2, 2014.

方向情報を考慮した細胞の力推定*

小沢 哲

内容梗概

細胞運動の原理を解明するため，細胞が発生する物理的力の計測が近年盛んである．代表的な実験的手法として，細胞の培養基質の表面に埋め込まれた蛍光ビーズを用いるものがあり，細胞の力は蛍光ビーズの変位データから推定する．しかし，物理的な制限により推定すべき力点の候補数よりも蛍光ビーズの数を抑える必要があるため，変位からの力推定は計算困難な逆問題である．この問題を解くために，本研究では細胞の形態と力ベクトルの方向に関する事前分布を用いたベイズ推定により，力を推定する手法を提案する．パラメータ推定にはEMアルゴリズムを利用した．本手法により力推定が劇的に改善されることを示す．

キーワード

ベイズ推定, VB法, EMアルゴリズム, 牽引力顕微鏡

*奈良先端科学技術大学院大学 情報科学研究科 情報科学専攻 博士論文, NAIST-IS-DD1161022, 2014年6月2日.

Contents

List of Figures

1. Introduction

Cell morphogenesis and migration are essential for various physiological and pathological processes, including metastasis and permeation of a cancer cell [1, 2], immune responses [3, 4], and precise wiring of intricate neuronal circuitry [5, 6, 7, 8, 9].

Kleeberger et al. investigated Nestin expression and function in common lethal cancers [1]. Their results specify a function for Nestin in cell motility and identify a novel pathway for prostate cancer metastasis. O'Hayre et al. indicated chemokines are involved in the progression of cancer [2]. One of the reasons is specific chemokine-receptor pairs are involved in tumor metastasis. This is not surprising, in view of their role as chemoattractants in cell migration.

Originally described as a T lymphocyte-derived factor that inhibited the random migration of macrophages, the protein known as macrophage migration inhibitory factor (MIF) was an enigmatic cytokine for almost 3 decades. In recent years, the discovery of MIF as a product of the anterior pituitary gland and the cloning and expression of bioactive, recombinant MIF protein have led to the definition of its critical biological role in vivo.

Recent studies have begun to analyze traction forces generated by non-neuronal [10, 11, 12, 13, 14] and neuronal [15, 16, 17, 18] cells, as cellular morphogenesis and migration depend on their ability to produce traction forces.

1.1 Force estimation methods

Traction force microscopy (TFM) is a framework to analyze the forces. TFM uses fluorescent nano beads that are embedded in the surface layer of an elastic gel substrate. When cells cultured on the substrate generate traction force, the beads change their locations due to the deformation of the gel substrate. The bead displacements can be quantified from time-lapse imaging data. Therefore, an important question is how to estimate cellular traction forces from bead displacements precisely.

1.1.1 Related works

Various algorithms have been proposed to estimate cellular traction forces [19]. The majority of previous studies introduce the equation of the forward model that converts forces to each bead displacement with the Boussinesq Green function with Poisson's ratio and Young's modulus of the substrate [20]. These studies introduced a computational mesh that is sufficiently smaller than the cell size. The boundary element method (BEM) is the first algorithm to estimate traction forces from bead displacements [21, 22]. The main results of this study are a transform the bead displacement field as an integral over the traction forces field and inversely solves the forward model with Tikhonov regularization. Fourier-transform traction cytometry (FTTC) [28] transforms the forward model to frequency space. Then the model can be written by simple matrix multiplication and the estimated forces are obtained to the multiple inverse matrix to the transformed bead displacements because the dimension of bead and force vector aligned through the DFFT process. 3D finite element methods [29] are also used to analyze bead displacement data. In general, cellular attachments to the substrate are formed at discrete regions within the cell. If such point-like positions of cellular attachments can be determined by microscopy, it is possible to estimate forces more precisely [30]. In addition, a high density of two different-colored nano beads improves the spatial resolution of the force estimation [31]. Sabass et al. compared BEM and FTTC in same settings, and reported the estimation accuracy of both methods is almost the same and the both methods occur underestimation [31].

1.2 Purpose of this thesis

In spite of such progress, there still remain problems in estimating the cellular forces. For example, when the number of marker beads is less than that of force points, calculating the force with the previous algorithms would become ill-posed. There is a limitation in the bead density, as the elastic property of the substrate would be disturbed by the high density of the beads. In addition, there are cases when it is difficult to measure point-like force positions due to experimental limitations. If these positions are unknown, estimated forces would be distributed widely to the place where cells do not exist [31]. Specifically, parameter con-

straints such as Tikhonov regularization make the forward model robust, but at the same time, they produce a large number of small forces. Conversely, with a weak constraint, a small number of larger forces are estimated. However, they may have low resistance to data noise. Therefore, it is useful to estimate forces with a moderate number of beads in a condition where point-like force positions are unknown.

In this study, I present a novel technique for estimating cellular force with a Bayesian framework. I use the previous observations that cells always generate forces inwardly by actin treadmilling [32, 33, 34, 35]. Using the Bayesian algorithm, I estimate the cellular forces of the synthetic dataset, which has low-density beads and unknown point-like forces. Bayesian force estimation shows high performance in estimating the cellular traction force compared with other previous algorithms.

1.3 Organization of Dissertation

In chapter 2, I explain how to estimate forces in the TFM framework. this chapter provides a fundamental information about TFM studies. In chapter 3, I explain about calculation of the bead displacements from the pair of bead images. In chapter 4, I describe my proposed force estimation method. Chapter 5 shows experimental results. Chapter 6 discusses the limits of my method and applications. I end this dissertation with chapter 7 which concludes my work and provides suggestions for future directions.

2. Traction force microscopy

Traction force microscopy (TFM) is a method to measure traction force of the cell adhesions. The basic idea of TFM dates back to the paper of Harris et al.[37]. They were the first to use a thin edible silicone sheet as wrinkling assay that gave a qualitative measure for the mechanical activity of cells Fig. 1. To see the location of the wrinkling of the sheets, one can know the locations where cells exert forces to the sheets.

A quantitative approach has been proposed by Iwadate et al. [23, 24]. They applied finite element method [25] to calculate gel stress field instead of forces directly. The method calculated gel strains and stresses on the mesh nodes (Fig. 2 (c)). The strains on meshes obtained from the bead displacements and the stresses obtained from the strains by normal physical calculation. In the normal finite element method, the size of the elements should be small and the density of the elements should be high in the area where the stress is expected to be large, while the size should be large and the density should be low in the area where the stress is expected to be small for accurate and fast calculation. In this study, however, small triangle meshes were distributed uniformly because the distribution of the stresses cannot be predicted. The accuracy of FEM based method highly depend on mesh size and mesh shapes. FEM requires fully observed gel displacement data, but gel displacement observed only on the beads. To solve this problem, they employ the displacements that were calculated as mean values of that of the neighboring beads.

An another quantitative methodology of TFM has been proposed by Dembo et al. [21, 22]. They use prestressed silicone gel rubber alternative silicone sheet, and can measure rubber deformations quantitatively to embed fluorescent beads into surface layer of the gel. The bead displacements calculate by capturing bead images with microscopy and image processing. To use bead displacements as observation data, cell traction forces are computed inversely. In this method, forces are estimated in some positions in the gel surface 2D-plane. The number of beads is finite and fewer than the number of force estimated position in most cases, then, the estimation is ill-posed problem. To solve this problem, they introduced the Bayesian framework and prior distribution.

Dembo's method is fundamental of TFM studies [28, 30, 31]. For example,

Fourier et al. [26] used a variant of Dembo's method that is computationally much faster [27].

In this chapter, I introduce details of forward model of the inverse problem that used Dembo and other TFM studies, and explain solving methods the problem.

2.1 Forward model

In traction force microscopy, beads are randomly scattered on the surface layer of the culture gel substrate, indicating that bead displacement is almost restricted in a 2D plane. Let us define $\mathbf{x} = [x, y]^t$ as the coordinate of the plane. When a cell produces a traction force, it deforms the substrate and displaces the beads (Fig. 3). The relationship between a given force and resultant bead displacement was modeled by Landau and Lifshitz [20]. If the bead displacement by the force, $\mathbf{f}(\mathbf{x})$, is written as $\mathbf{u}(\mathbf{x}) = [u_x(\mathbf{x}), u_y(\mathbf{x})]$, it can be formulated by using

$$\mathbf{u}(\mathbf{x}) = \int_{\Omega} G(\mathbf{x} - \mathbf{x}')\mathbf{f}(\mathbf{x}')\mathrm{d}\mathbf{x}' \tag{1}$$

$$G(\mathbf{x}) = \frac{1+\nu}{\pi E r^3} \begin{bmatrix} (1-\nu)r^2 + \nu x^2 & \nu xy \\ \nu xy & (1-\nu)r^2 + \nu y^2 \end{bmatrix}, \tag{2}$$

where ν and E are the Poisson ratio and Young's modulus, respectively. Σ is a area of interest to calculate displacement. The Poisson ratio and Young's modulus describe physical characteristics of gel substrates and can be calculated from the substrates. The purpose of TFM is to estimate force $\mathbf{f}(\mathbf{x})$ from displacement $\mathbf{u}(\mathbf{x})$.

In implementation, I discretized forces and displacement in this model. So I can estimate forces on only finite mesh grid. The number of the grid is limited by the number of bead displacement because if the number of the grid is smaller than the number of beads, this problem become ill-posed problem. In real settings, however, the number of force grid I would like to know is more than the number of beads.

2.2 Boundary element method (BEM)

Measurements of substrate deformation, even if they are very accurate, are merely secondary reflections of the biologically generated tractions. Therefore, to deduce

the actual traction stresses being exerted upon a substratum point by point it is necessary to process the information inherent in displacement measurements by some sort of statistical procedure. To calculate of such traction images, Dembo et al. [21] approximate the distribution of traction stresses acting on the substratum as superposition of elementary delta function influences.

The main result of Boundary element method (BEM) [21] is representing the bead vector $\mathbf{u}$ by the sum of the forces. To estimate force vector, I solve this model inversely. The problem is ill-posed because the number of force estimated points larger than the number of beads in most cases. To solve this problem BEM method introduced Tikhonov regularization scheme. The estimated force $\hat{\mathbf{f}}(\mathbf{x})$ is obtained to minimize the following objective function:

$$||\mathbf{u}(\mathbf{x}) - \Sigma_{\mathbf{x}'} G(\mathbf{x} - \mathbf{x}')\mathbf{f}(\mathbf{x}')||^2 + \lambda||\mathbf{f}(\mathbf{x})||^2. \tag{3}$$

This method frequently occurs underestimation due to the regularization term.

2.3 Fourier-transform traction cytometry (FTTC)

Butler et al. describe the foundations of Fourier transform traction cytometry (FTTC), a new and computationally efficient method for computing the traction field given the displacement field [28]. FTTC divides into two subclasses (unconstrained and constrained), described below, and in several respects are fundamentally different from the BEM method. The first key difference is that the BEM method requires the cell boundary to be drawn by hand and constrains the tractions exterior to the boundary to be zero while still retaining approximate matching of the exterior displacements. By contrast, unconstrained FTTC exactly matches all the displacement data, independent of the perceived cell boundary; constrained FTTC forces the tractions exterior to the cell boundary (drawn by hand) to be zero, as in the BEM method, but ignores the exterior displacement data. The second key difference is that the BEM approach utilizes Tikhonov regularization with a particular choice and intensity of smoothing functional. By contrast, FTTC utilizes no smoothing and is exact in the sense that it yields a traction map for which the induced displacements exactly match the given displacement field.

FTTC transformed the forward model to the frequency space. Transformed force $\tilde{\mathbf{f}}$ and displacement $\tilde{\mathbf{u}}$ are expressed by following equation:

$$\tilde{\mathbf{u}}(\mathbf{v}) = \tilde{G}(\mathbf{v})\tilde{\mathbf{f}}(\mathbf{v}) \tag{4}$$

where $\tilde{G}$ is the converted Green function G of Eq. (1) to the frequency space.

Then the degrees of freedom of the traction and the displacement are aligned. The transformations of displacement $\mathbf{u}$ can be done with standard techniques for fast Fourier transform (FFT), and inverting FFT also applies to transform the obtained $\tilde{\mathbf{f}}$ to real space. The use of the FFT-algorithm to compute the Fourier transform of the displacement field requires a regular, rectangular grid covering the whole image, which is obtained from irregular fields by biquadratic interpolation.

2.4 3D TFM

3D TFM is the 3D-force estimation method from fully observed 3D-displacement field [36]. This method can be calculated without any assumption or restriction, but this is required the bead displacement fully observed in 3D space.

First, submicron-sized fluorescent particles are embedded within the transparent biomaterial of interest and three-dimensional time-lapsed volumetric images are recorded using laser scanning confocal microscopy (LSCM). Next, cell-induced material deformations (i.e., displacements) are calculated using a recently developed digital volume correlation (DVC) algorithm that tracks the center displacement of individual spatial subsets of the recorded LSCM images in all three dimensions. Once the full-field displacements are obtained the three-dimensional strain tensor ϵ is calculated using a displacement-gradient method. To calculate the cell-induced three-dimensional full-field stresses or the stress tensor (σ), the material properties (e.g., Young's modulus and Poisson's ratio) or the material's constitutive behavior need to be determined through independent mechanical testing. Finally, cell-applied traction forces can be directly calculated along any plane (represented by its normal vector ($\mathbf{n}$)),within the material as well as on its surface, by simple matrix multiplication of the normal with the material stress tensor as follows:

$$T \ = \sigma \cdot \mathbf{n}. \tag{5}$$

As the schematic illustrates, this method does not rely on any mathematical frameworks or stress-state assumptions, such as the Boussinesq theory or FEM analysis. Because all material displacements can be calculated from three-dimensional LSCM images, the tractions can be calculated in a forward way based solely on mechanics principles as described in detail in the following sections. This obviates the need for any inverse formulation and stabilization schemes that are generally necessary for 2D TFM calculations.

Although this method required fully displacement field in the interest region, the method can calculate traction field by simply matrix multiplication.

2.5 Issue of related works

FTTC and 3D TFM methods require fully observed bead displacement data. A advantage of these methods is their can be calculated the traction force without any assumption if once the displacement data obtained because they don't have ill-poseness. However, it is difficult to obtain the fully observed displacements because no bead area has no information about displacement. Some displacement estimation method can be estimate the displacement in such area, but the estimated displacements have error with large value frequently.

BEM can use only the displacements around beads, but the method occurred underestimation [31]. The reason of the underestimation is effect of the prior that have effect of shrunk to the traction forces.

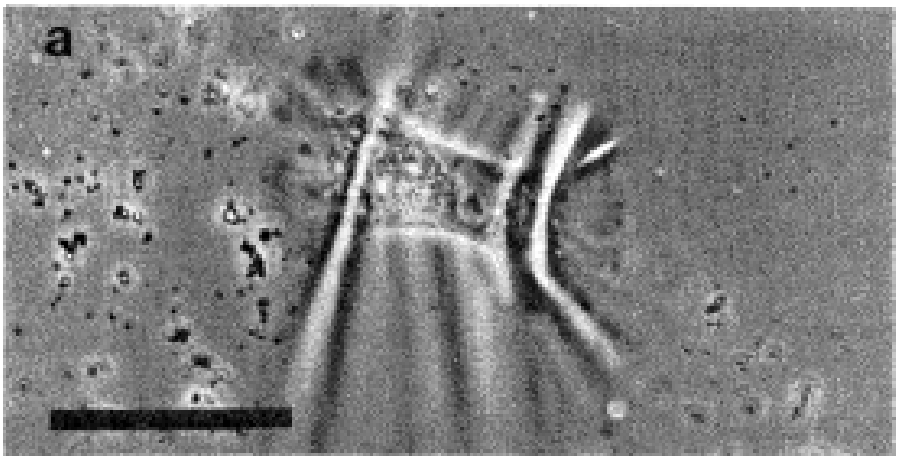

Figure 1. A microscopic image that is captured in a cell, which is an individual heart fibroblast, on a silicone rubber seat [37]. Vertical lines are wrinkles of the seat. The bar is $50\mu m$ long. The wrinkles are made by the cell forces, so that one can know where the cell exert forces by seeing the wrinkled locations.

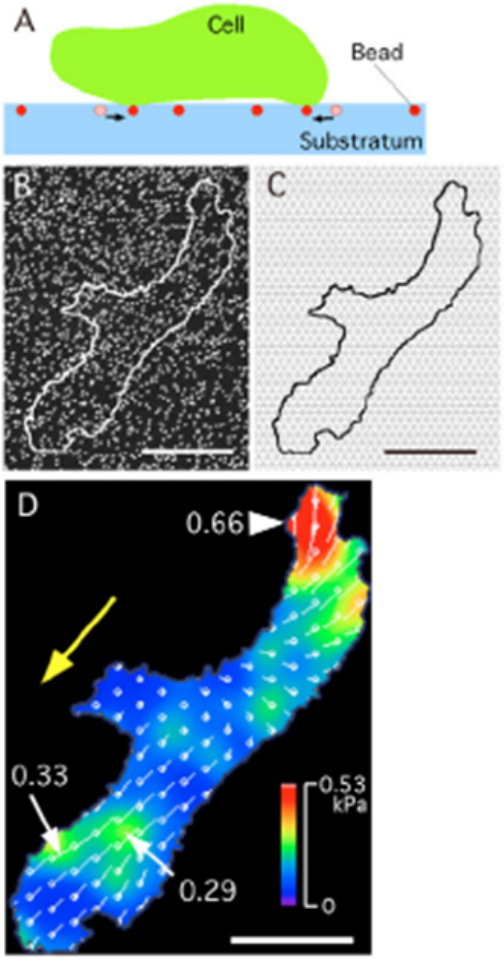

Figure 2. Schematic drawing of Iwadate methods [24]. (a) Experimental setting. A Cell addressed on a gel surface. The cell exerted forces on the gel, and gel deformed by the forces. The gel displacements are observed as bead displacements. In this method, the cell stresses obtained from bead displacements. (b) Bead image. The white dots are beads in gel surface, and the white line is cell edge. (c) Mesh map. Gel strains and stresses of the gel are calculated on the nodes of the meshes. The mesh shape is uniform triangle. (d) The estimated force map. The stresses are calculated on the white circles and the white lines on the circles indicate direction and magnitude of the stresses. The yellow line indicates the direction of cell migration. The color map represents magnitude stresses. This figure shows cell moves to the direction on which is distributed weak stresses.

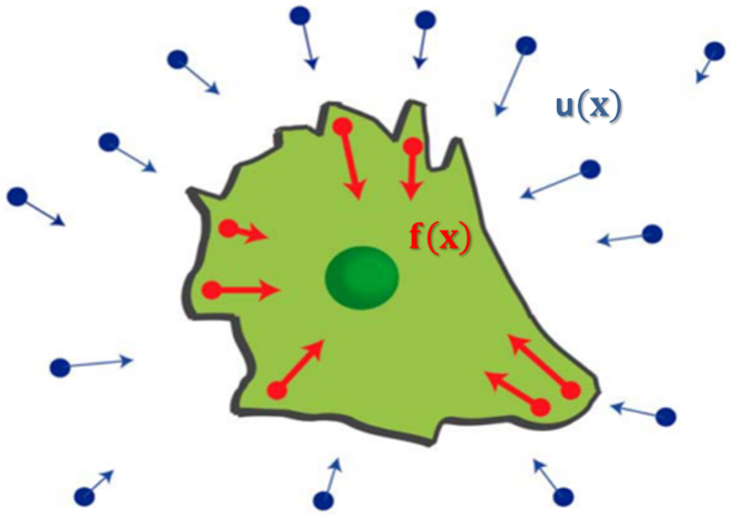

Figure 3. Experimental setting of TFM [31]. This shows cell on the gel as top view. The forces, which are red arrows, exerted on the red points, and the beads, which are represented as blue points, move as blue arrows. Bead displacements $\mathbf{u}(\mathbf{x})$ can be calculated from traction forces $\mathbf{f}(\mathbf{x})$ with the forward model Eq. (1). TFM is a method to estimate the forces from the bead displacements.

3. Calculation of the bead displacement

3.1 Introduction

In this chapter, I explain the method to extract bead displacement from consecutive two beads embedded images. To extract the bead displacements, I referred to the optical flow estimation methods in the computer vision area.

Optical flow is the motions of the objects in a scene and is typically expressed with the vector field that moves the objects to the position in the next scene. In this study, I used the flow field as bead displacements field. Optical flow estimation is the methods to extract such fields from two images in consecutive scenes. To estimate optical flow, Horn and Schunck [38] assume the condition that image intensity on a point of one image equals to that on the matched point of the other image. The condition expressed as follows:

$$I_1(\mathbf{x}) \quad = I_2(\mathbf{x} + \mathbf{u}), \tag{6}$$

where $I_i (i \in \{1, 2\})$ is image intensity, $\mathbf{x} = [x, y]^t$ is a coordinate in 2-D plane and $\mathbf{u} = [u_x, u_y]^t$ is the flow vector. In addition, Horn and Schunck added a regularization term to improve robustness to observation noise. As a result, the optical flow estimation was formulated as a such objective function minimization problem:

$$\underset{\mathbf{u} \in \mathbb{R}^2}{\operatorname{argmin}} \, ||I_1(\mathbf{x}) - I_2(\mathbf{x} + \mathbf{u})|| + (\mathit{regularization\ term}). \tag{7}$$

$\operatorname{argmin}_{\mathbf{x}} f(\mathbf{x})$ returns set of $\mathbf{x}$ that minimize the function $f(\mathbf{x})$. If $f(\mathbf{x})$ is a quadratic function, $\operatorname{argmin}_{\mathbf{x}} f(\mathbf{x})$ returns a value of $\mathbf{x}$. Various methods have been developed based on this equation and such methods is called the variational framework. Variational framework is often occurred bad estimation when the true displacements are large, due to inadequateness of the linear approximation. So, the variational framework is unsuitable for estimating the bead displacement because the large bead displacement often occurred by the cell adhesion in my setting.

Optical flow estimation also formulated as point (or descriptor) matching problem by Brox et al. [39]. In my study, this approach was introduced, and the bead centroids were treated as the descriptors. The reason is no bead area of the

bead image is no informative to estimate displacements, so I avoid to add noise to estimate the displacements in the such areas.

Brox et al. also said about the reasons of descriptor matching has not been a success story as follows:

- "The most successful descriptors are all based on spatial histograms. Histograms are not well localized, and thus the precision of the motion estimates, especially at motion discontinuities, is lower than with, e.g., variational techniques."

- "Although most descriptors can be uniquely matched between images, some of them are confused or their counterpart in the other image is missing due to occlusions. This causes a certain amount of mismatches that are very disturbing for most optical flow applications."

- "Descriptor matching is a discrete technique, which only allows for pixel accuracy. This quantization effect prevents distinguishing small motions and causes drift in tracking applications."

The first problem can avoid to add the position constraint to matching cost function as follows:

$$\underset{\mathbf{u}\in\mathbb{R}^2}{\operatorname{argmin}} \left\| \frac{I_1(\mathbf{x}) - I_2(\mathbf{x}+\mathbf{u})}{(maxIntensity)} \right\| + \|\mathbf{x} - (\mathbf{x}+\mathbf{u})\|, \tag{8}$$

where $I_i (i \in \{1,2\})$ is image intensity and $\{\mathbf{x}, \mathbf{x}+\mathbf{u}\}$ are locations in each images. The second problem can be translated that "overlapped beads problem" in my setting (shown in Fig. 4). The overlapped beads cannot estimate easily because it is difficult to judge which bead is overlapped or not. I focused on the diameter of each bead is almost same and modeled the bead image as summation of synthetic bead-patch with fixed diameter. I will explain the details in the next section. To overcome the third problem, I provided the set of candidates of one bead centroid, and defined the coordinate of the centroid as the mean of its positions. So, I can estimate bead displacements with sub-pixel accuracy.

3.2 Formulation of bead detection as linear problem

I formulated bead detection problem as a linear problem (Fig. 5). Let us define $\mathbf{x}$ as a bead image, A as a matrix that column represents synthetic bead images and each of element of $\mathbf{b}$ represents position of the synthetic bead image . In this formulation, I assumed the synthetic bead size is fixed to 4 pixel. The mean of bead diameters in real setting (described in chapter 5) is roughly 200nm, and the length of a side of the pixel is roughly 100nm. Thus, the real bead diameter is 2 pixels in reality, but beads are blurred in microscope image. That's why I employed 4 pixels as diameter of synthetic bead image.

I can get the positions of the beads to solve this linear problem.

I show the result of this problem with three linear problem solvers (Least squares, Lasso [40], Dantzig Selector [41]) in Fig. 6. Dantzig selector is better than other methods to extract bead positions. Especially, an advantage of Dantzig selector is its result have value only on the beads, in constant that of other two method have value not only beads. Then I choose the Dantzig selector as a solver of this problem.

3.3 Least squares methods

Least squares method is a mathematical procedure for finding the best-fittings lines to a given set of points by minimizing the sum of the squares of the residuals as follows.

$$\underset{\mathbf{b}}{\operatorname{argmin}} ||\mathbf{x} - A\mathbf{b}||_2^2. \tag{9}$$

The sum of the squares of the residuals is used instead of the offset absolute values. This method is easy to implement because the cost function can be differentiated analytically, and the optimal solution is written as follows:

$$\hat{\mathbf{b}} = (A^t A)^{-1} A^t \mathbf{y}. \tag{10}$$

In my setting, the number of parameters $\mathbf{x}$ is larger than the number of observations $\mathbf{y}$, so $A^t A$ often becomes singular matrix. the inversion of the matrix don't exist. There are several way to approximate the inversion numerically, but one should take care of the error of the calculate.

Prediction error $||\mathbf{y}-A\hat{\mathbf{b}}||^2$ can be decomposed to two terms, bias and variance. Both of terms are represented about property of the bias term is represented with the mean value of the error in some data, and the variance term is represented with the variance of the data. Least squares method is often referred as high bias and low variance method, that is, estimator of the least squares method is stable by difference of data sample, but the estimator has some error in anytime.

3.4 Ridge regression

Ridge regression estimate method with subject to shrinkage parameter vector $\mathbf{b}$ to 0.

The ridge regression is formulated as following:

$$\underset{\mathbf{b}}{\operatorname{argmin}} ||\mathbf{x} - A\mathbf{b}||_2^2 + \lambda||\mathbf{b}||_2^2 \tag{11}$$

The difference to the Least squares is that the ridge regression add to penalty term to shrink the parameter. λ is the hyper-parameter to control the effect of the 2nd term. If λ is zero, the ridge regression is equal to least squares.

The estimator of ridge regression is represented as following form:

$$\mathbf{b} = (A^tA + \lambda I)^{-1}A^t\mathbf{y} \tag{12}$$

In mathematics sight of view, $(A^tA + \lambda)$ is full rank symmetric matrix, then the matrix have inverse matrix when $\lambda \neq 0$ and ridge regression can be calculate the estimated vector without some approximation.

However, the estimated vector is not interpretable, that the vector don't have some zero elements, because both term of the ridge regression are quadratic cost function. Especially, in my setting, I would like to find the locations of beads. I hope that the element of the vector correspond to no-bead area fill close to 0.

3.5 LASSO (Least Absolute Shrinkage and Selection Operator)

The LASSO [40] is a linear regression method that is penalized by sum of the absolute value of the parameters. By penalizing of the term, the LASSO tends

to produce some parameters that are exactly 0 and results of the method are interpretable. In other words, we can specify the set of parameters that effect to the model.

The LASSO is formulated as follows

$$\underset{\mathbf{b}}{\operatorname{argmin}} ||\mathbf{x} - A\mathbf{b}||_2^2 + \lambda||\mathbf{b}||_1, \tag{13}$$

where λ is the parameter controls the effect of the second term on the optimization.

The LASSO also have another form as following:

$$\underset{\mathbf{b}}{\operatorname{argmin}} ||\mathbf{x} - A\mathbf{b}||_2^2 \text{ s.t. } ||\mathbf{b}||_1 < \epsilon, \tag{14}$$

where ϵ is the parameter corresponding to λ in the above equation. This equation indicates some elements of the estimated vector $\mathbf{b}$ tends to be 0 compared with LS and Ridge regression, because the optimized vector is in a diamond area in p-dimensional Euclidean space made by the term $||\mathbf{b}||_1 < \epsilon$, where p is the dimension of the vector $\mathbf{b}$.

3.6 Dantzig selector

Dantzig selector [41] is a estimator to overcome ill-posedness that the number of variables or parameters, p, is much larger than the number of observations, n. Dantzig selector is a solution to the $\ell 1$-regularization problem

$$\underset{\mathbf{b}}{\operatorname{argmin}} ||\mathbf{b}||_1 \text{ s.t. } ||A^*(\mathbf{x} - A\mathbf{b})||_\infty < \epsilon \tag{15}$$

The objective function of Dantzig selector evaluates $A^*(\mathbf{x} - A\mathbf{b})$ instead of $\mathbf{x} - A\mathbf{b}$. One of the reasons is invariance to orthonormal transformation. Suppose $\mathbf{b}' = U\mathbf{b}$ where $I = UU^*$. $A^*(\mathbf{x} - A\mathbf{b})$ equals to $A^*(\mathbf{x} - A\mathbf{b}')$. Then the Dantzig selector don't depend on U.

3.7 Short results: effect of the fixed diameter beads

To confirm the legality of my detection approach, I compared detection result with a bead detection method (spot detector) that used in TFM area [42]. My

method and spot detector applied to a bead image. The results are shown in Fig. 8. In Fig. 8, my method with Dantzig selector can detected beads in dense bead areas by comparison with the spot detector.

Fig. 9 shows proposed approach have capability of catch each overlapped bead position, in constant spot detector treat the overlapped-beads as a lump bead. In addition, proposed approach don't detect the beads embedded in deeper space. That beads occur estimation error in the force estimation and, detection of that beads are unstable each images due to darkness than other beads.

To validate detection performance quantitatively, I evaluated 3 methods (proposed with Dantzig selector and LASSO, and spot selector) with true positive and false positive ratios using a image (Fig. 7 (a)). In this thesis, true positives represent detected points on bead areas correctly and false positives represent detected points on no bead ares. Then, true positive and false positive ratios defined that

$$true\ positive\ ratio = \frac{\#\ of\ true\ positives}{the number\ of\ beads} \tag{16}$$

$$false\ positive\ ratio = \frac{\#\ of\ false\ positives}{the\ pseudo\ \#of\ no\ bead\ area\ blocks}. \tag{17}$$

To obtain the denominator of the true positive ratio, the image labeled by hand (Fig. 7 (b)). The number of labels are the denominator of the true positive ratio. In this image, the number of the no beads areas cannot count correctly (the denominator of the false positive ratio). To obtain the pseudo number of the no bead area, I calculate the ratio of the bead and no bead areas of Fig. 7, and then I defined the pseudo number of the no bead area as following:

$$\#\ of\ no\ bead\ areas = the\ ratio\ beads\ and\ no\ beads \cdot \#\ of\ beads. \tag{18}$$

From true positive and false positive ratio, I illustrated result with ROC curve (Fig. 10). Each point represent detection result of 3 methods with different hyper parameters (λ in Eq. (13) and ϵ in Eq. (15)). In ROC curve, left top is best performance because the point has high true positive ratio and low false positive ratio. Fig. 10 shows that my methods with Dantzig selector detected beads more than LASSO version and the spot detector.

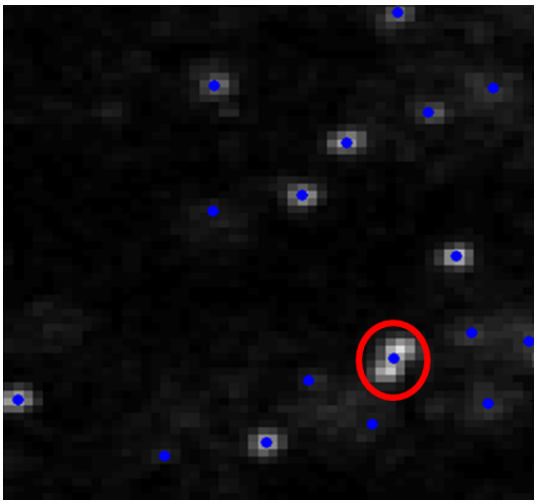

Figure 4. Bead image that have overlapped beads (red circle). Blue points are detected bead points.

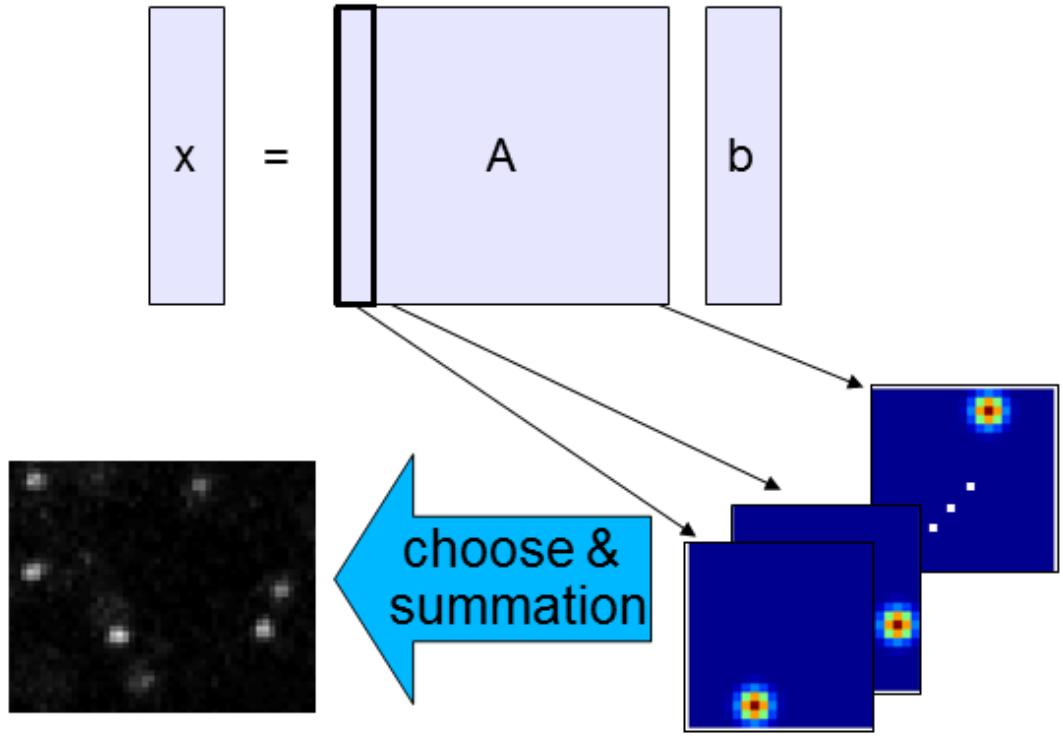

Figure 5. Beads detection model. I suggested a summation of synthetic bead images model. To estimate the weight vector **b** of this model, beads locations are detected.

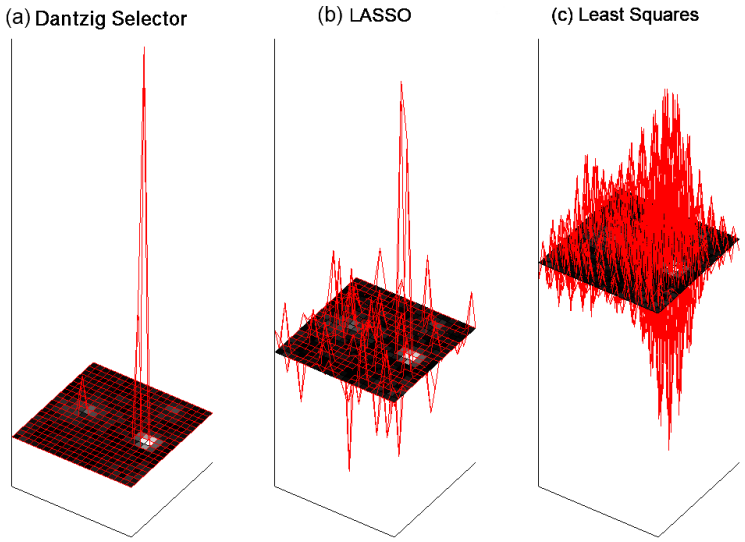

Figure 6. Estimated weight vectors of Dantzig selector (a), LASSO (b) and Least squares (c). The red lines that represent estimated weight vectors $\mathbf{b}$ are overlaid on the bead image. The weight vector of Dantzig selector represents beads location exactly.

(a)

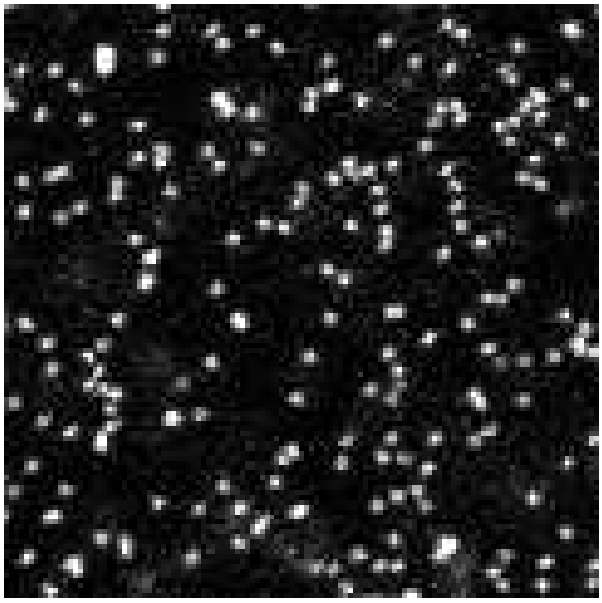

(b)

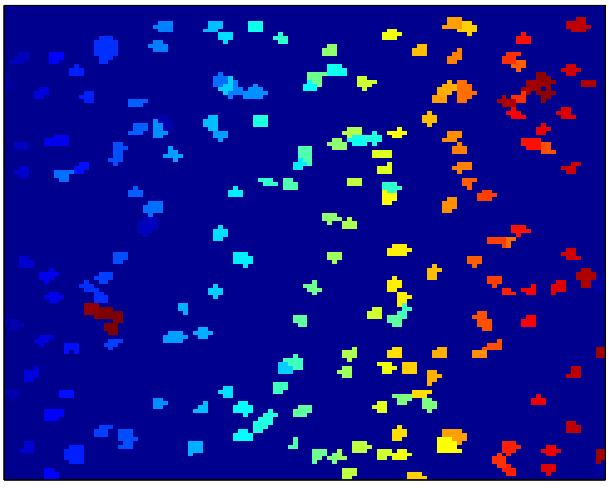

Figure 7. Bead image (a) and the labeled image (b). The images prepared to evaluate proposed detection method and spot detector. In the labeled image, each other colored areas indicates the bead area that have another label.

(a)

(b)

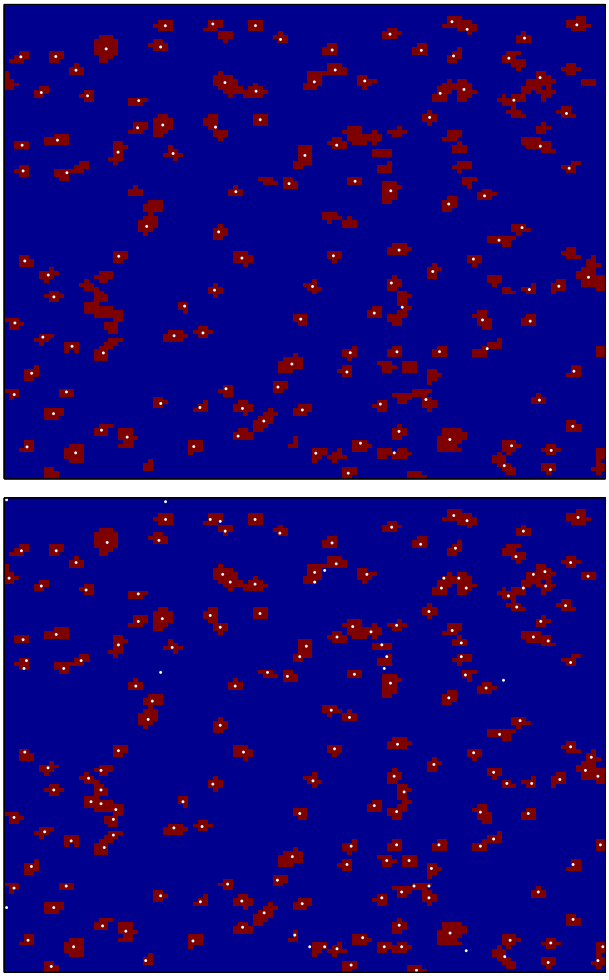

Figure 8. Bead detection results with spot detector (a) and proposed approach (b). The detection positions (white dots) are overlapped on the binarized bead image. The advantage of proposed approach especially arises in dense bead areas.

(a)

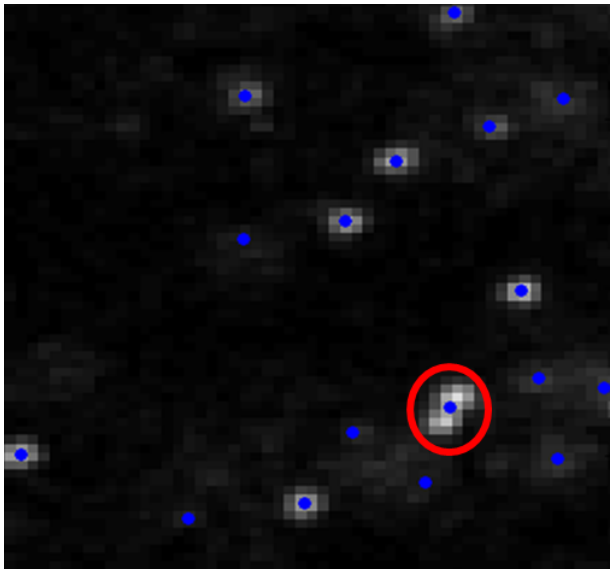

(b)

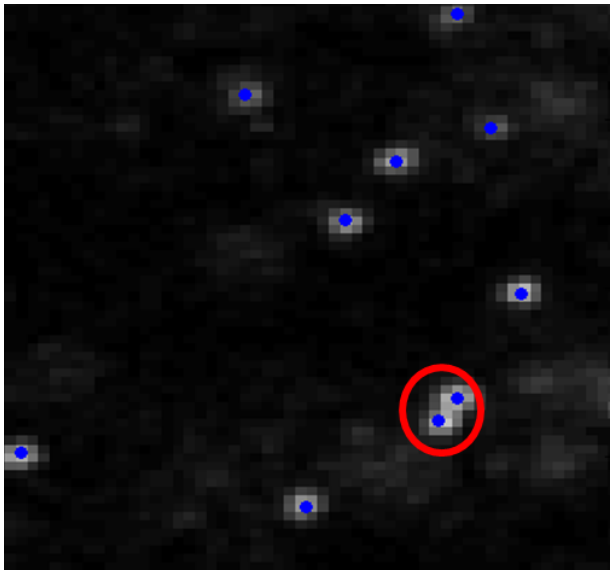

Figure 9. Bead detection results with spot detector (a) and proposed approach (b). The blue point is the detected points in each method. Proposed method can be obtained overlapped beads in red circle and don't detect in background areas.

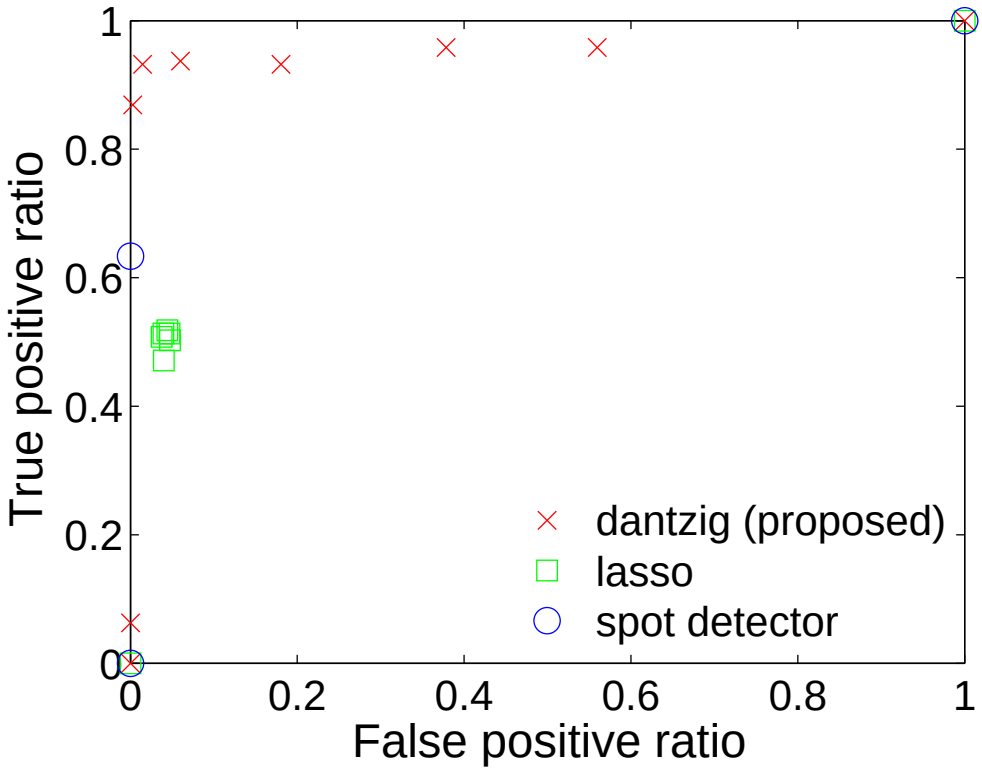

Figure 10. ROC curves of beads detection task from one image with Dantzig selector (red), LASSO (green) and spot detector (blue). False positive of the spot detector is close to zero. In other word, spot detector doesn't catch no-bead areas as bead areas. However, beads detection rate (true positive) is lower than Dantzig selector. In Dantzig selector, false positive is low and true positive is high. Then, this picture shows Dantzig selector is best performed in this task.

4. Proposed force estimation method

4.1 Introduction

In this chapter, I explain our model and the optimization method. At first, I will show a little example to show difficulty of the force estimation problem. Fig. 11 is a estimation result from real data with three methods. The methods are BEM, FTTC and Dantzig selector. Fig. 11 shows the estimated forces raised only on the beads positions. The reason is the Green function in Eq. (1) is so localized and then the estimated force raised only on the beads if the number of beads is insufficient. This phenomenon is a serious issue because I cannot know true force site.

There are two way to overcome this issue: the number of beads increasing and the number of force decreasing. The beads increasing way is often tried in TFM area. However, the way also have the follow issues:

- difficulty of beads detection in dense beads area.
- effect to the physical property of the gel-substrate.

Especially, the effect of the latter is unpredictable then I not use this way. The decreasing way don't also use because I cannot know true force position in this way.

I introduce a novel method that introduce the force-centripetal point. It determines force direction toward the point. Then I can estimate only force amplitude and the centripetal point. So, the effect of introducing the point is the skipping estimation of the force directions. In other words, the dimension of force vector I should estimate is decreased to a half.

I extended the model to multi centripetal points. In next section, I will explain the model and the way of how to estimation parameters.

4.2 Generative model

Let us define $\mathbf{x} = [x_n, y_n]^t$ as the coordinate of the n-th force action point and $\mathbf{c}_k = [c_{kx}, c_{ky}]^t$ $(k = 1, \ldots, K)$ as the coordinate of the k-th force-centripetal point. I suppose that each force belongs to one of the force-centripetal points (Fig. 12).

Since the definition of $\mathbf{c}_k$ prescribes only the direction of the forces, their amplitudes are independent from the locations of $\mathbf{c}_k$. Considering these restrictions, I can formulate the model force at $\mathbf{x}$, which points to the k-th centripetal point by using

$$\mathbf{f}_k(\mathbf{x}) = r_k(\mathbf{x})\,(\mathbf{c}_k - \mathbf{x}) + \mathbf{n}_{\mathbf{f}k}(\mathbf{x}), \tag{19}$$

where $\mathbf{n}_{\mathbf{f}k}(\mathbf{x})$ is the noise term that represents fluctuations in the direction and amplitude of the force and obeys the 2-D Gaussian distribution $N(\mathbf{f}(\mathbf{x})|\mathbf{0}, \alpha^{-1}I)$ with a known hyperparameter, α. The coefficient, $r_k(\mathbf{x})$, is estimated from the bead displacement around $\mathbf{x}$ and does not correspond to a spring constant. Here, I introduce a hidden binary variable, $z_k(\mathbf{x})$, that represents which centripetal-point $\mathbf{f}(\mathbf{x})$ points to; $z_k(\mathbf{x}) = 1$ if $\mathbf{f}(\mathbf{x})$ belongs to $\mathbf{c}_k$, and $z_k(\mathbf{x}) = 0$ otherwise. Using $z_k(\mathbf{x})$, $\mathbf{f}(\mathbf{x})$ can be expressed as,

$$\mathbf{f}(\mathbf{x}) = \prod_{k=1}^{K} \left(r_k(\mathbf{x})\,(\mathbf{c}_k - \mathbf{x}) + \mathbf{n}_{\mathbf{f}k}(\mathbf{x})\right)^{z_k(\mathbf{x})}. \tag{20}$$

On the basis of this formulation, I provided a prior distribution for $z_k(\mathbf{x})$ as described in the next section.

The relationship between a force and bead displacement was modeled as Eq.(1). To treat this model in Bayesian framework, I added a noise term, $\mathbf{n}_{\mathbf{u}}(\mathbf{x})$, as follows

$$\mathbf{u}(\mathbf{x}) \;=\; \int_{\Omega} G(\mathbf{x} - \mathbf{x}')\mathbf{f}(\mathbf{x}')\mathrm{d}\mathbf{x}' + \mathbf{n}_{\mathbf{u}}(\mathbf{x}). \tag{21}$$

$\mathbf{n}_{\mathbf{u}}(\mathbf{x})$ obeys the Gaussian distribution, $N(\mathbf{n}_{\mathbf{u}}(\mathbf{x})|\mathbf{0}, \beta^{-1}I)$, with the known hyperparameter β. Eq. (1) is the observation model, and I use this for calculating likelihood. The relationship of the variables and parameters represented graphically in Figs. 13 and 14.

4.3 Transformation to probabilistic model

Using the generative model described as Eqs. (20) and (1), I estimate $\mathbf{f}(\mathbf{x})$, $z_k(\mathbf{x})$, $r_k(\mathbf{x})$, and $\mathbf{c}_k$ from the observation of the bead displacement, $\mathbf{u}(\mathbf{x})$. Because it is difficult to estimate these parameters in a continuous space, the gel substrate

needs to be discretized. If the location on the substrate is discretized to $\mathbf{x}_n$ $(n = 1, \ldots, N)$, I can replace Eq. (20) to the discretized probability distribution of $\mathbf{f} \equiv [f_{1x}, f_{1y}, \ldots, f_{nx}, f_{ny}]^t$ conditioned by $\mathbf{z}$ with

$$P(\mathbf{f}|\mathbf{z}) = \prod_{n=1}^{N} \prod_{k=1}^{K} N(\mathbf{f}_n | r_{nk}(\mathbf{c}_k - \mathbf{x}_n), \alpha^{-1} I)^{z_{nk}}. \tag{22}$$

The probability distribution of $\mathbf{z}$ is given by using

$$P(\mathbf{z}|\pi) = \prod_{n=1}^{N} \prod_{k=1}^{K} \pi_k^{z_{nk}} \tag{23}$$

$$P(\pi) = \mathrm{Dirichlet}(\pi|a_0) = C(a_0) \prod_{k=1}^{K} \pi_k^{a_0 - 1}, \tag{24}$$

where $C(\cdot)$ is the normalization term, and the random variable, π_k, is the occurrence frequency for $z_k = 1$. The hyperparameter, a_0, is given as a small number (< 1), by which $\mathbf{f}(\mathbf{x})$ belongs to only one centripetal point. In this paper, I set a_0 to 0.1.

For the observation model, by using the discretized location of a bead, $\mathbf{x}_i$ $(i \in N_i \subset \{1, \ldots, N\})$, we have

$$\begin{aligned} \mathbf{u}_i &\equiv \mathbf{u}(\mathbf{x}_i) \\ G_i &\equiv [G(\mathbf{x}_i - \mathbf{x}_1), \ldots, G(\mathbf{x}_i - \mathbf{x}_N)] \\ \mathbf{f} &\equiv [\mathbf{f}(\mathbf{x}_1), \ldots, \mathbf{f}(\mathbf{x}_N)]\,. \end{aligned}$$

Then, the likelihood function of Eq. (1) can be replaced to

$$P(\mathbf{u}_i|\mathbf{f}) \;\; = N(\mathbf{u}_i | G_i \mathbf{f}, \beta^{-1} I). \tag{25}$$

Using the priors (Eqs. (22)-(24)) and the likelihood (Eq. (25)), the posterior distribution,

$$P(\mathbf{f}|\mathbf{u}, \mathbf{z}, \pi) \propto P(\mathbf{u}_i|\mathbf{f}) P(\mathbf{f}|\mathbf{z}) P(\mathbf{z}|\pi) P(\pi), \tag{26}$$

is defined.

4.4 Calculation for optimized solution

It is practically impossible to calculate Eq. (26) analytically, so I approximate it by using the Variational-Bayes method. I introduce a trial distribution, $q(\mathbf{f}, \mathbf{z}, \pi)$,

that maximizes the variational-energy function,

$$F(q) = \iiint q(\mathbf{f}, \mathbf{z}, \pi) \ln \frac{p(\mathbf{u}, \mathbf{f}, \mathbf{z}, \pi | r, c)}{q(\mathbf{f}, \mathbf{z}, \pi)} \mathrm{d}\mathbf{f}\mathrm{d}\mathbf{z}\mathrm{d}\pi. \tag{27}$$

The trial distribution, q, is known as the approximation of $p(\mathbf{f}, \mathbf{z}, \pi | \mathbf{u})$ since the maximization of the variational-energy function with respect to q is equivalent to the minimization of the Kullback-Leibler divergence between $p(\mathbf{f}, \mathbf{z}, \pi | \mathbf{u})$ and $q(\mathbf{f}, \mathbf{z}, \pi)$. Although q can be an arbitrary distribution for unknown variables $\mathbf{f}$, $\mathbf{z}$, and π, for the sake of tractability, I assume that it can be factorized as

$$q(\mathbf{f}, \mathbf{z}, \pi) = q(\mathbf{z}) q(\mathbf{f}, \pi).$$

By this assumption, the optimal trial distribution, $q^*(\mathbf{f}, \mathbf{z}, \pi) = q^*(\mathbf{z}) q^*(\mathbf{f}, \pi)$, that maximizes Eq. (27) is analytically given as

$$\begin{aligned}
q^*(\mathbf{z}) &= \prod_{n=1}^{N} \prod_{k=1}^{K} m_{nk}^{z_{nk}} && (28) \\
q^*(\mathbf{f}, \pi) &= q^*(\mathbf{f}) q^*(\pi) \\
q^*(\pi) &= \mathrm{Dirichlet}(\pi | \mathrm{a}) && (29) \\
q^*(\mathbf{f}) &= N(f | \mu_{\mathbf{f}}, \Sigma_{\mathbf{f}}), && (30)
\end{aligned}$$

where

$$\begin{aligned}
m_{nk} &= \frac{\rho_{nk}}{\sum_j \rho_{jk}} && (31) \\
\ln \rho_{nk} &= \mathbb{E}[\ln \pi_k] - \ln(2\pi) + \ln \alpha - \frac{\alpha}{2} \mathbb{E}\left[\| \mathbf{f}_n - r_{nk}(\mathbf{c}_k - \mathbf{x}_n) \|^2 \right] && (32) \\
\mathrm{a} &= [a_1, \ldots, a_k, \ldots, a_K]^t && (33) \\
a_k &= a_0 + \sum_n m_{nk} && (34) \\
\Sigma_{\mathbf{f}} &= \left(\beta \sum_i G_i^t G_i + \alpha I \right)^{-1} && (35) \\
\mu_{\mathbf{f}} &= \Sigma_{\mathbf{f}} \left(\beta \sum_i G_i^t \mathbf{u}_i + \alpha \sum_k M_k R_k (\mathbf{c}_k - \mathbf{x}) \right) && (36) \\
M_k &\equiv \mathrm{diag}(m_{1k}, m_{1k}, \ldots, m_{Nk}, m_{Nk}) && (37) \\
R_k &\equiv \mathrm{diag}(r_{k1}, r_{k1}, \ldots, r_{kn}, r_{kn}). && (38)
\end{aligned}$$

I take $\mu_{\mathbf{f}}$ in Eq. (36) as the estimation of $\mathbf{f}$.

The unknown parameters, R_k and $\mathbf{c}_k$, remain to be estimated and cannot be obtained analytically. I numerically estimated these parameters by using the expectation-maximization (EM) algorithm. The approximated force, $\mu_{\mathbf{f}}$, (Eq. (36)) is calculated in the E-step, while in the M-step, I compute R_k and $\mathbf{c}_k$, by which the error function,

$$\begin{aligned} F(R, \mathbf{c}) &= \mathbb{E}\left[\sum_n \sum_k z_{nk} \|\mathbf{f} - R_k(\mathbf{c}_k - \mathbf{x})\|^2\right] \\ &= \sum_n \sum_k m_{nk} \|\mu_{\mathbf{f}} - R_k(\mathbf{c}_k - \mathbf{x})\|^2, \end{aligned} \tag{39}$$

is minimized. From the necessary condition,

$$\begin{aligned} \frac{\partial F}{\partial r_{nk}} &= -2m_{nk}(\mu_{\mathbf{f}nx} - r_{nk}(c_{kx} - x_n))(c_{kx} - x_n) \\ &\quad -2m_{nk}(\mu_{\mathbf{f}ny} - r_{nk}(c_{ky} - y_n))(c_{ky} - y_n) = 0 \\ \frac{\partial F}{\partial c_{kx}} &= -2\sum_n m_{nk}(\mu_{\mathbf{f}nx} - r_{nk}(c_{kx} - x_n))r_{nk} = 0 \\ \frac{\partial F}{\partial c_{ky}} &= -2\sum_n m_{nk}(\mu_{\mathbf{f}ny} - r_{nk}(c_{ky} - y_n))r_{nk} = 0, \end{aligned}$$

I obtain

$$\hat{r}_{nk} = \frac{\mu_{\mathbf{f}nx}(c_{kx} - x_n) + \mu_{\mathbf{f}ny}(c_{ky} - y_n)}{(c_{kx} - x_n)^2 + (c_{ky} - y_n)^2} \tag{40}$$

$$\hat{c}_{kx} = \frac{\sum_n m_{nk}\mu_{\mathbf{f}nx} r_{nk} + m_{nk} x_n r_{nk}^2}{\sum_n m_{nk} r_{nk}^2} \tag{41}$$

$$\hat{c}_{ky} = \frac{\sum_n m_{nk}\mu_{\mathbf{f}ny} r_{nk} + m_{nk} y_n r_{nk}^2}{\sum_n m_{nk} r_{nk}^2}. \tag{42}$$

Due to the constraint $r_{nk} \geq 0$, r_{nk} is set to zero if $r_{nk} < 0$. By repeating the E- and M-step described above, $\mathbf{f}(\mathbf{x})$, $r_k(\mathbf{x})$, and $\mathbf{c}_k$ converge to stable values.

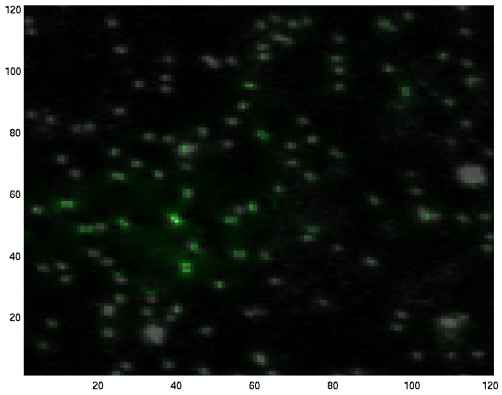

(a)

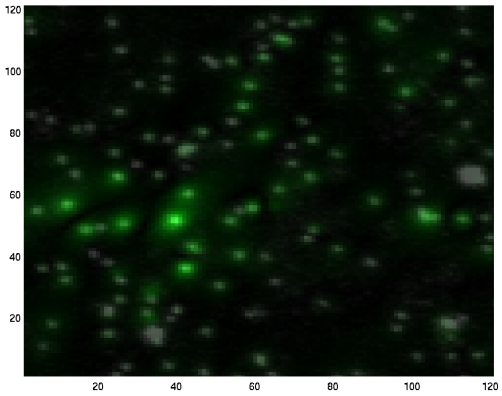

(b)

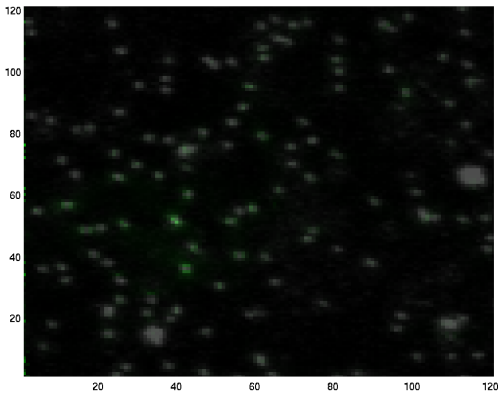

(c)

Figure 11. Estimated results with BEM (a), FTTC (b) and Dantzig selector (c). The green represents the amplitude of the estimated forces and the white is the beads.

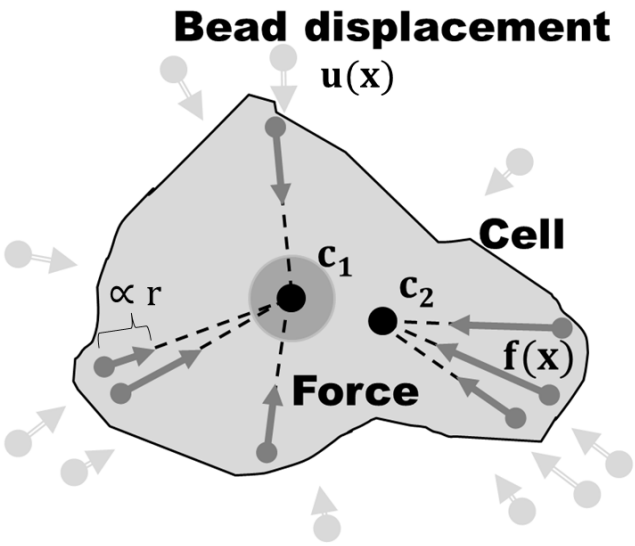

Figure 12. Prior knowledge considered force direction. Biological cells always produce inward forces. This fact can be modeled by introducing the force-centripetal points ($\mathbf{c}_1$ and $\mathbf{c}_2$), which all of the forces ($\mathbf{f}$) point to. r is proportional force magnitude. That is, r is considered the parameter represent force magnitude.

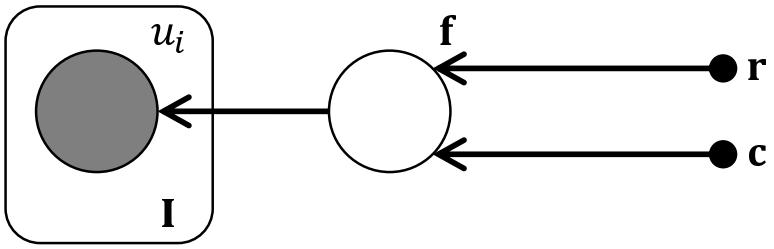

Figure 13. Graphical model of the proposed method with single afferent point. I would like to obtain force **f** from observation **u**. r and c are treated as just parameters, and estimated with EM algorithms.

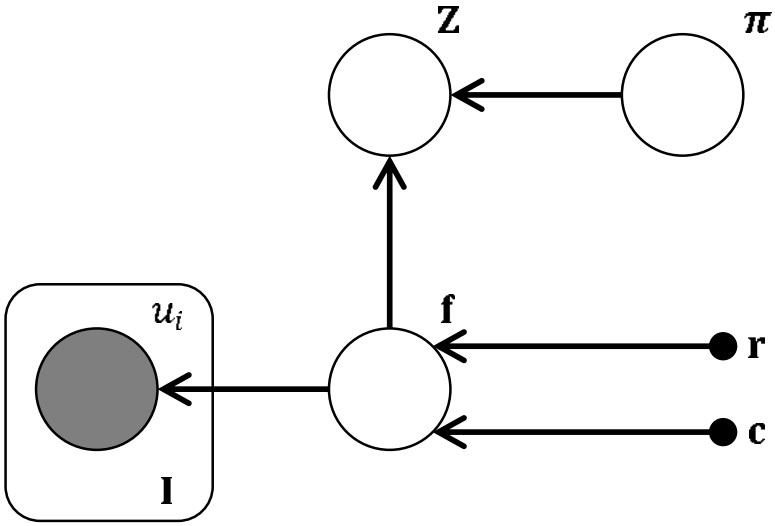

Figure 14. Graphical model of the proposed method with multi afferent point. I would like to obtain force **f** from observation **u**. **z** and π are the variables to regulate the rates of the effects of each afferent point on each point force. r and c are treated as just parameters, and estimated with EM algorithms.

5. Experiments

This chapter show two synthetic data result and one real data result. To test the effectiveness of our Bayesian approach, we analyzed synthetic images and compared the results with the BEM method [31]. In Real data, I show the validity to apply our method to real settings.

5.1 Synthetic image for single centripetal point

I provided a synthetic image with the following steps.

- The virtual image was subdivided by 30×30 grid lines, and a single centripetal point, $\mathbf{c}$, was defined as one of grid intersections.
- Ten forces were generated on the basis of Eq. (20) at the locations distributed around $\mathbf{c}$. The amplitudes were randomly chosen.
- 200 beads were distributed randomly over the image, and the bead displacement, $\mathbf{u}$, was calculated from Eq. (1) with $\mathbf{f}$s.
- Finally, 15 [dB] noise was added to $\mathbf{u}$ (Fig. 15).

Using the synthetic image, I compared our approach with ridge regression [21, 22](Fig. 16). The error was evaluated by using the mean square error between the estimated and the synthetic forces. Since ridge regression gave a good estimation only if a sufficiently large number of bead measurements is given, our Bayesian approach was superior to ridge regression with a smaller number of beads. This result suggests that by using our method, it is possible to estimate cellular force precisely even with less beads. The error of the Bayesian approach slightly increased in the range of a large number of beads. This may be due to an over-fitting phenomenon.

To validate the locality of the estimated force distribution, I compared the estimated forces by using both approaches with different numbers of beads (Fig. 16). When the numbers of beads were both 150 and 800 beads, the Bayesian approach succeeded in estimating the local forces, whereas ridge regression failed and scattered forces around the true forces. Moreover, as shown in Fig. 18, the Bayesian

approach could detect a force even if the bead density was locally low. It was difficult for ridge regression to detect a force in such a condition.

5.2 Synthetic image for multiple centripetal points

Most biological cells have a complicated morphology and change their shape dramatically in order to sense the external environment and move to a target direction. In such a realistic case, there must be multiple force centripetal points. I applied our algorithm to another synthetic image that was generated in the same way as the single centripetal point but had multiple centripetal points. Each force points to one of the centripetal points.

The simulation results for the data of two centripetal points are shown in Fig. 17. The algorithm with two centripetal points succeeded in estimating forces with small errors (Fig. 17a). In addition, the locations of the centripetal points were also well estimated. Apparently, forces could not be estimated properly if the algorithm with a single centripetal point was applied (Fig. 17b). In the ridge regression algorithm, the error became larger, and in particular, the localities of the cellular forces failed to be estimated (Fig. 17 c).

To check the advantages of the algorithm as well as the data in Fig. 16, I computed the estimation errors for the data of two centripetal points with the ridge regression and the Bayesian algorithm (Fig. 18). I estimated the forces with various parameter values of centripetal points in the Bayesian algorithm. As a result, the Bayesian force estimation showed better performance than did the ridge regression. Even if the parameter of the centripetal points in the Bayesian algorithm was larger than that of the bead displacement data, all of the centripetal points converged to one of two points of the data.

5.3 Real data experiments

I applied our method to real neuronal cell images to confirm validity for real datasets. To test effectiveness in real data, I compared estimated forces from real cell data. The data is obtained by Dr. Toriyama, which is my collaborator. To explain the property of the data, I cited his paper [18] to the next section for convenience.

5.3.1 Experimental procedure

Cell Culture, Transfection, and RNAi Hippocampal neurons prepared from E18 rat embryos were cultured on glass coverslips (Matsunami) coated with L1-CAM-FC as described [43]. All experiments except for the measurement of forces were carried out on L1-CAM-coated glass surfaces. Neurons were transfected with plasmid DNA using Nucleofector (Lonza) before plating. For RNAi experiments, to ensure a high level of expression of miRNA before axon outgrowth, neurons were cultured in suspension on non-coated polystyrene dishes for 24 h [44], and then collected and seeded onto coated-glass coverslips, polyacrylamide gels, or glass bottom dishes. For the immunoblot analyses in Figures 2B, S4D, and S4E, we used cortical neurons, which also respond to Netrin-1 [45], as the experiments required large numbers of neurons. These were prepared from E18 rat embryos using the same protocol as above. For RNAi experiments, we used a Block-iT Pol II miR RNAi expression kit (Invitrogen). The targeting sequence of shootin1 miRNA was reported previously [44]; that of another miRNA (shootin1 RNAi # 2), 5 ' -GTTAGAGGAACGGCTAGAGAA-3 ' , corresponds to nucleotides 867-887 in the coding region of rat shootin1. Reduction of endogenous shootin1 in neurons was confirmed by immunocytochemistry with anti-shootin1 antibody.

DNA Constructs Preparation of the vectors to express wild-type shootin1 has been described previously [44]. RNAi-refractory shootin1 mutants were generated using a QuickChange II site-directed mutagenesis kit (Stratagene) as described [43]. Unphosphorylated (S101A/S249A: AA) or phosphomimic (S101D/S249D: DD) mutants of shootin1 were generated with the same kit, to replace each serine with alanine or aspartate, using the following primers: S101A,
5'-CGTTGAAAAGAATCGCCATGTTGTACATGGCCAAGCTGGGACC-3 ' ; S101D,
5'-CGTTGAAAAGAATCGACATGTTGTACATGGCCAAGCTGGGACC-

3 ' ; S249A,
5'-CAAGCTAAAGAGACAAGCCCACCTTCTGCTGCAGAGCTCCATC-3 ' ; and S249D,
5'-CAAGCTAAAGAGACAAGACCACCTTCTGCTGCAGAGCTCCATC-3 ' .
cDNAs were sub-cloned into pGEX-6P-1 (GE Healthcare), pEGFP-C1 (Clontech) and pCMV-myc-3B (Stratagene). Pak1 plasmids were kindly provided by Drs. M. Inagaki and L. Lim. Constitutively active Pak1 (CA-Pak1) was described previously [46]. The autoinhibitory domain (AID; aa 83-149) of Pak1 and its mutant AID-L107F were used as dominant negative Pak1 (DN-Pak1) and control, respectively, as reported previously [47]. Plasmids for constitutively active Cdc42, Rac1, and RhoA [48] were kindly provided by Dr. K. Kaibuchi.

Protein and Antibody Preparation Recombinant shootin1 was expressed in Escherichia coli as a GST fusion protein and purified on a Glutathione Sepharose column (GE Healthcare), after which GST was removed from shootin1 by PreScission protease (GE Healthcare). L1-CAM-FC was prepared as described [43]. Polyclonal antibodies against shootin1 phosphorylated at Ser101 (anti-pSer101-shootin1 antibody) and Ser249 (anti-pSer249-shootin1 antibody) were raised by immunizing rabbits with the synthetic phosphopeptides TLKRI[pS]MLYMC and KLKRQ[pS]HLLLC, respectively. The antibodies were purified using a phosphopeptide affinity column, and absorbed by non-phosphopeptide affinity column to ensure their specificity [49]. Preparation of anti-shootin1 antibody has been described previously [44]. Netrin-1 and Tuj1 were obtained from R&D Systems and Covance, respectively.

In Vitro Kinase Assay Kinase reactions were carried out in 120 μl kinase buffer (50 mM HEPES (pH 7.5), 10 mM $MgCl_2$, 2 mM $MnCl_2$, 1 mM DTT, 10μ C_i [$\gamma-^{32}$P]ATP, and 25μ M ATP) containing 50 ng active GST-Pak1 (Invitrogen) and 250 ng purified shootin1-WT or its unphosphorylated mutants. After incubation at 30°C for 30 min, the

reactions were stopped by adding 5x SDS sample buffer and boiled. The reaction mixtures were subjected to SDS-PAGE and analyzed using autoradiography and Coomassie Brilliant Blue staining.

Immunocytochemistry, Immunoblot, and Microscopy Cultured neurons were fixed with 3.7% formaldehyde in Krebs buffer for 10 min at room temperature, followed by treatment for 15 min with 0.05% Triton X-100 in PBS on ice and 10% fetal bovine serum in PBS for 1 h at room temperature. They were then stained with antibodies and Alexa-594 phalloidin (Invitrogen), as described [43]. Immunoblot was performed as described [44]. Fluorescence and phase-contrast images of neurons were acquired using a fluorescence microscope (Axioplan2; Carl Zeiss) equipped with a plan-Neofluar 40x 0.75 NA or 63x oil 1.40 NA objective (Carl Zeiss), a charge-coupled device camera (AxioCam MRm; Carl Zeiss), and imaging software (Axiovision3; Carl Zeiss). The length of filopodia and axons, and the relative fluorescence intensity of shootin1 or F-actin, were measured using Multi Gauge software (Fujifilm). Fluorescent speckle imaging and speckle tracking analysis were performed as described previously [43].

Rac1 and Cdc42 Activity Assays Rac1 and Cdc42 activity assays were performed as described [50]. Cells were lysed with GSH-FISH buffer (50 mM Tris-HCl (pH 7.5), 100 mM NaCl, 2 mM $MgCl_2$, 10% glycerol, 1% NP-40, 2 mM phenylmethylsulfonyl fluoride, and 2 μg/ml leupeptin) and centrifuged for 15 min at 17,400 g at 4°C. The supernatants were incubated with 2 μg of GST-Pak1-CRIB protein bound to Glutathione Sepharose 4B for 90 min at 4°C. The beads were washed three times with GSH-FISH buffer and bound proteins were eluted in 1x SDS sample buffer. Bound Rac1 and Cdc42 were analyzed by immunoblot using anti-Rac1 (Upstate Group) or anti-Cdc42 (BD Transduction Laboratories) antibodies.

Traction Force Microscopy Polyacrylamide gel substrates were prepared as reported [51, 52, 53], with slight modifications. Briefly, glass bottom dishes (No. 0, Matsunami) were treated with 0.1 N NaOH for 15 min and incubated with 2% (v/v) 3-aminopropyltrimethyoxysilane (Sigma) in 2-propanol for 15 min. After washing with H_2O, 0.5 % glutaraldehyde (Sigma) solution was dropped onto the glass and incubated for 30 min. The glass bottom dishes were then washed with H_2O and dried before use. The acrylamide and Bis-acrylamide stock solutions (Nacalai tesque) were diluted to 3.75% and 0.03%, respectively, as reported [53]. Five hundred μl of solution was degassed for 30 min, and then 50 μl of fluorescent microspheres (2% solid, 200 nm diameter; Invitrogen), 1 μl of 10% (w/v) ammonium persulfate (GE Healthcare), and 1 μl of N,N,N,N-tetramethyl ethylenediamine (Nacalai Tesque) were added to initiate polymerization. Twenty-five ?l of the mixture was immediately pipetted onto 18-mm glass coverslips (No. 1, Matsunami) and the previously treated glass bottom dishes were placed, inverted, on the coverslips. After polymerization, the glass coverslips were peeled off and the surfaces of the gels were covered with H_2O to prevent drying until use. Sulfo-SANPAH (1 mM; Pierce) was dropped onto the gels, which were then exposed to UV light under sterile conditions for 5 min, and washed three times with 0.1 M HEPES (pH 7.5) for 15 min. The gel surfaces were coated with 0.1 mg/ml poly-D-lysine (Sigma) overnight, anti-FC antibody (Jackson) for 3 h, and finally with L1-CAM-FC overnight. The stiffness of the polyacrylamide gels was determined using a microsphere indentation method [52]. Briefly, a steel ball (0.6 mm diameter, 7.87 g/cm^3 ; Sato Tekkou) was placed on the gels embedded with fluorescent beads. The indentation caused by the steel ball was measured using a microscope. Young' s modulus was obtained as $E = 3(1-\nu^2)f/4d^{\frac{3}{2}}r^{\frac{1}{2}}$, where f is the buoyancy-corrected weight of the steel ball, d is the indentation of the gel, r is the radius of the steel ball, and v is the Poisson' s ratio (whose value is 0.3, as determined previously [54]). The Young' s modulus was 269.42 $\pm$ 24.17 N/m^2 (mean $\pm$ SE, n =

7). Time-lapse imaging of fluorescent beads and growth cones was performed at 37°C using a confocal microscope (LSM700 or LSM710; Carl Zeiss) equipped with a plan-Apochromat 63x 1.40 oil M27 objective. The growth cone area was determined from EGFP fluorescence or DIC images. In all analyses, we measured bead displacement under the peripheral domain (including filopodia and lamellipodia) and the central domain of axonal growth cones but not under the axonal shaft. After observation, the glass bottom dishes were treated with 1% SDS to release neurons from the polyacrylamide gel substrate, and an image of the unstrained substrate was acquired.

5.3.2 Results of real data

From a time-lapse beads images, I obtained beads displacement data as described chapter 3. The beads displacement data used to estimate force with proposed force estimate method and BEM. The hyper parameters of propoed method determined as $a = 0.1, \alpha = 0.1$ and $\beta = 1$. The hyper parameter of BEM determined as $\lambda = 0.1$.

The magnituge of estimated forces by two methods (proposed method, BEM) is shown in Fig. 19. This result shows us the advantage of our method because estimated forces are addressed on the cell edge in our approach.

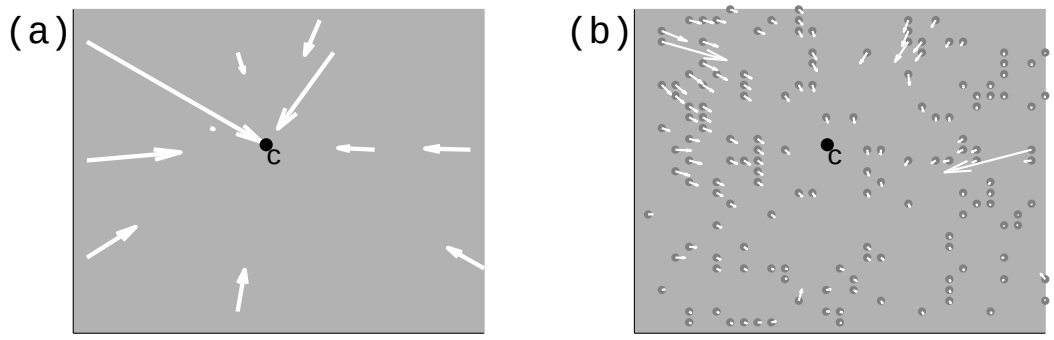

Figure 15. Example of synthetic force (**a**) and bead displacement (**b**). Arrows represent forces or bead displacements. Gray points are bead locations. Black points are centripetal points.

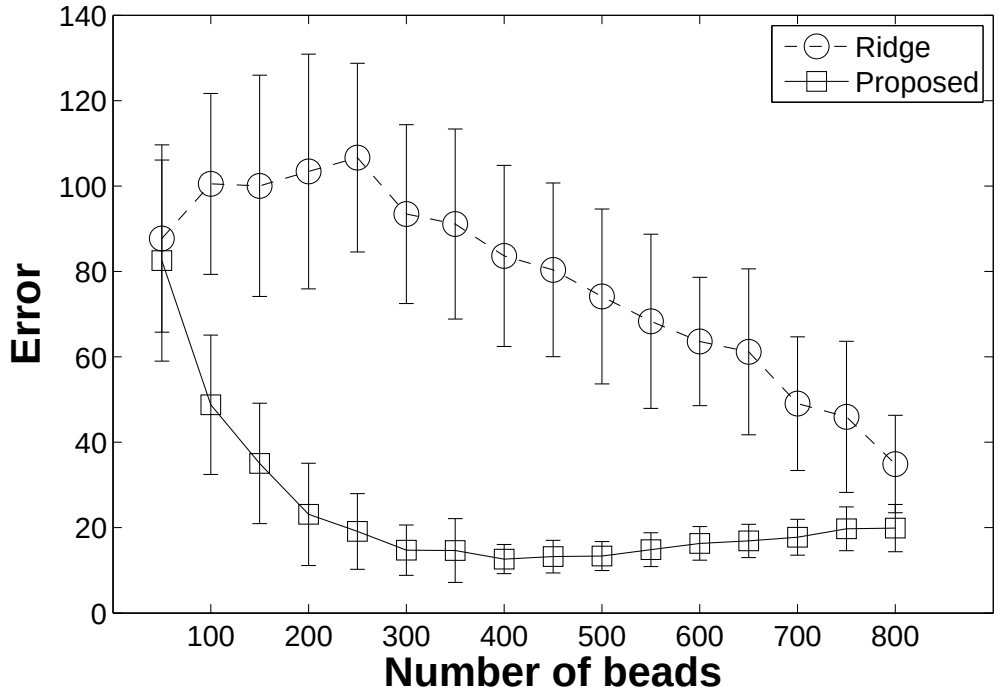

Figure 16. Comparison between estimation errors with Bayesian approach and ridge regression. The error was evaluated with the mean square error between the estimated and the synthetic forces for 50 trials. Error bars represent s.d.

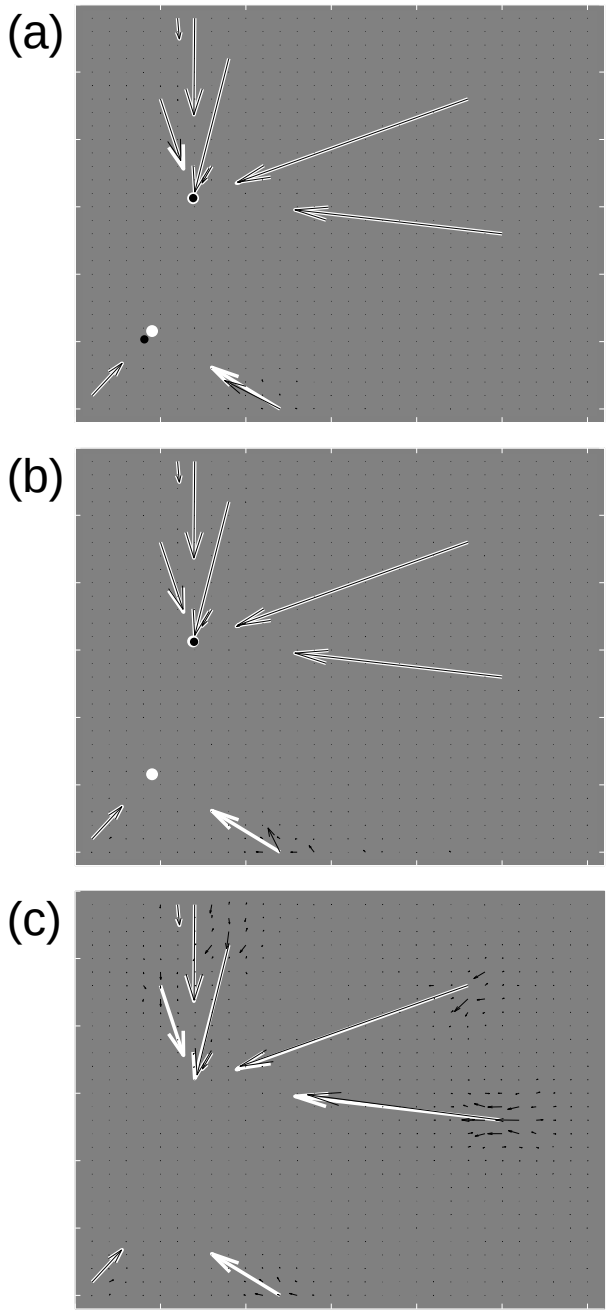

Figure 17. Estimation results of two-centripetal-point estimation (**a**), single-centripetal-point estimation (**b**), and ridge regression (**c**). White and black filled circles represent true and estimated centripetal points.

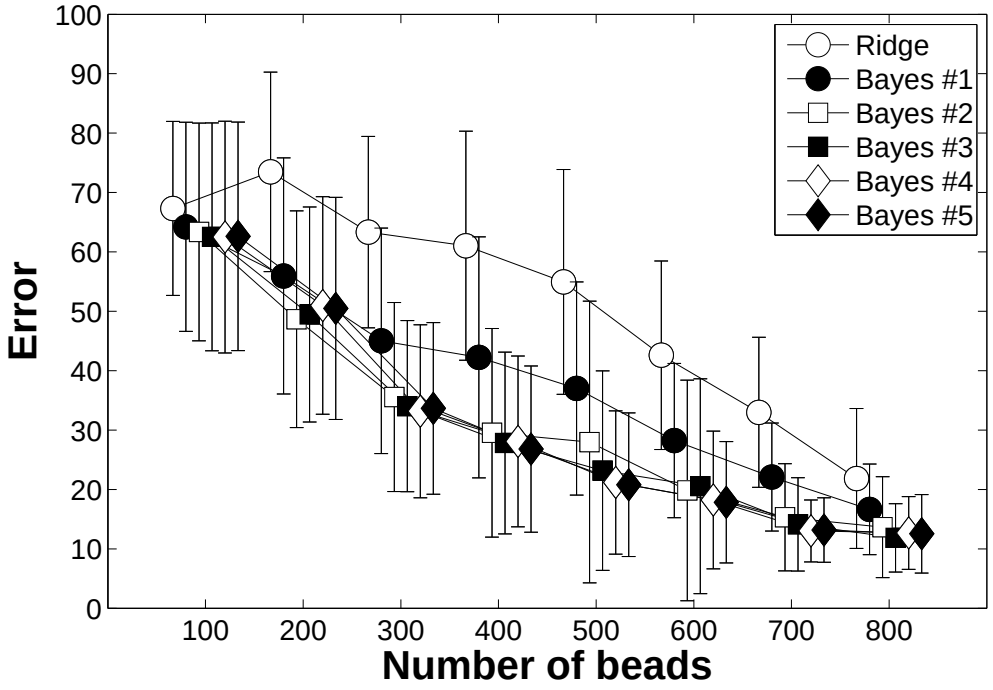

Figure 18. Comparison between force estimation errors with the ridge regression and five Bayesian algorithms for the datasets of two-centripetal-points. The numbers with a symbol # represent the estimated centripetal points in the Bayesian algorithms. Error was evaluated with the mean square error between the estimated and synthetic forces for 50 trials. Error bars represent s.d.

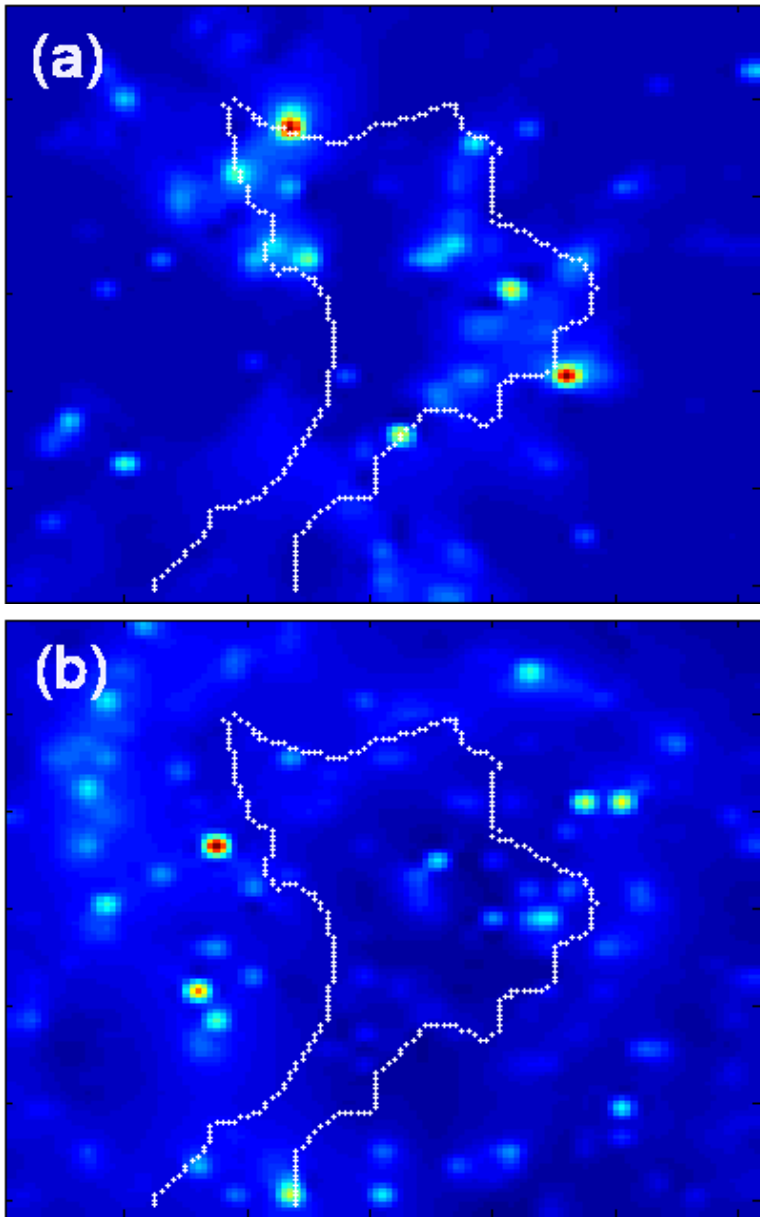

Figure 19. Estimated forces of our approach (**a**) and BEM method (**b**) for real cell data. White lines represent cell edges.

6. Discussion

The results show that our proposed method has the ability to estimate the force that no-bead area. In the synthetic experiment, the proposed had lower error than the ridge regression method in any number of beads data. The most difference between the proposed method and the ridge regression method is the force reconstruction of the lower or less beads areas. In the real data experiment, the estimated force of the proposed is interpretable, that is, the forces are distributed on the cell edges. These are effects of the centripetal-points, that is, the points choice the information to on purpose.

The proposed method used Bayesian framework same as the ridge regression method. Bayesian framework provides the probabilistic distribution of the forces, then one can see not only the estimated forces, but the dependability of the forces in each element of the force vectors. The disadvantage of the proposed method is that parameter sensitivity is very high, and inappropriate parameter soccers the centripetal point go away. I have to discover an appropriate parameter search method in the hyper parameters.

The estimated results of the proposed methods have information about that forces are assigned which centripetal-point. If a centripetal-point represents the center of a cell, we can know which cell exerted a force of interest to see the information in multi cell setting. It may be helpful to understand the interaction of the cells.

My study has been focused on the forces in the 2-D plane of the cells that exert force to extracellular matrix, but my force estimation method can extend to the 3-D force. In this study, the observation is the 2-D beads image deformed by the cell force and the observation model is a 2-D version. The observation model can be extended to 3-D version easily, then, 3-D force estimation achieved if I can get 3-D observation data. However, No adhesion cell, such as floating cell, cannot estimate force by the proposed approach. To estimate the force exerted by such cells, I should incorporate more information, for example, the morphology of the cell, flow of the Liquid cultures, molecular activities and so on. To incorporate such information, Bayesian framework is so useful. Actually, in this thesis, I incorporated 2 models, gel model and inward force assumption, using Bayesian framework. The prior distribution of this thesis is described in the directions of

vectors. The prior can apply to some problem class using vector field.

7. Conclusion

In this study, I tried to develop new the cellular force estimation method. I achieved this by a Bayesian approach that estimates cellular force from the displacements of fluorescent nano beads even under low-density bead and unknown force point conditions. These results suggest that prior knowledge of force directions provides robust force estimation instead of Tikhonov regularization. Answering the question of how to determine the number of centripetal points is future work; however, I will be able to solve this by using model selection algorithms such as variational Bayes. By using this methodology, I can estimate the cellular force with more accuracy and contribute to biological experiments.

This study is a solver of TFM force estimation approach to object improvement of the estimation accuracy. A application of force estimation is prediction of the cell shapes. To improve the estimation accuracy, the prediction accuracy is also improved.

Acknowledgements

To complete this study, I am grateful to the following respected people. First and foremost, I express my gratitude to my supervisors, Professor Kazushi Ikeda and Associate Professor Yuichi Sakumura, who gave suggestive advice and invaluable support. I also express my gratitude to my collaborators, Associate Professor Naoyuki Inagaki and Dr. Michinori Toriyama, who gave good discussion and experiment data. I express my obligation to the other staff of our laboratory. Dr. Takatomi Kubo and Dr. Hiroyuki Funaya directed specic methods of analysis. Dr. Takashi Takenouchi, Dr. Kazuho Watanabe and Dr. Tomoya Tamei gave me valuable comments to improve my study. Our secretary, Ms. Aya Tanimoto, Ms. Satomi Adachi assisted my study to be accomplished comfortably, including adminis- tration for conducting experiments and publications. In addition, I greatly ap- preciate lots of support given by graduates of our laboratory. Keiko Teramura suggested a marvelous idea which served as a stimulus to diligence. Satoshi Nishida taught me how to conduct the experiments including how to operate an eye tracker. Finally, I would like to express special thanks to my colleagues, Kei Majima and Tatsuya Yamada, for great support in daily life.

References

[1] Kleeberger, W., Bova, G. S., Nielsen, M. E., Herawi, M., Chuang, A. Y., Epstein, J. I., Berman, D. M., (2007) Roles for the Stem Cell-Associated Intermediate Filament Nestin in Prostate Cancer Migration and Metastasis, Cancer Res. 67(19), 9199–9206.

[2] O'Hayre, M., Salanga, C. L., Handel, T. M., Allen, S. J., (2008) Chemokines and cancer: migration, intracellular signalling and intercellular communication in the microenvironment, Biochem. J. 409, 635–649.

[3] Calandra, T. and Bucala, R., (1997) Macrophage Migration Inhibitory Factor (MIF): A Glucocorticoid Counter-Regulator within the Immune System, Critical Reviews in Immunology, 17, 77–88.

[4] Luster, A. D., Alon, R., von Andrian, U. H., (2005) Immune cell migration in inflammation: present and future therapeutic targets, Nature Immunology, 6, 1182–1190.

[5] Edmondson, J. C. and Hatten, M. E., (1987) Glial-guided granule neuron migration in vitro: a high-resolution time-lapse video microscopic study, J. Neurosci. 7(6), 1928–1934.

[6] Tessier-Lavigne, M. and Goodman, C. S., (1996) The molecular biology of axon guidance, Science 274, 1123–1133.

[7] Ma, Q., Jones, D., Borghesani, P. R., Segal, R. A., Nagasawa, T., Kishimoto, T., Bronson, R. T., Springer, T. A., (1998) Impaired B-lymphopoiesis, myelopoiesis, and derailed cerebellar neuron migration in CXCR4- and SDF-1-deficient mice, Proc. Natl. Acad. Sci. USA, 95(16), 9448–9453.

[8] Dickson, B. J., (2002) Molecular mechanisms of axon guidance., Science 298, 1959–1964.

[9] Charron, F., Tessier-Lavigne, M., (2005) Novel brain wiring functions for classical morphogens: a role as graded positional cues in axon guidance, Development 132, 2251–2262.

[10] Beningo, K. A. and Wang, Y-L, (2002) Flexible substrata for the detection of cellular traction forces, Trends Cell Biol. 12, 79–84.

[11] Roy, P., Rajfur, Z., Pomorski, P., Jacobson, K., (2002) Microscope based-techniques to study cell adhesion and migration., Nat. Cell Biol. 4, E91–E96.

[12] Rieu, J. P., Barentin, C., Maeda, Y., Sawada, Y., (2005) Direct Mechanical Force Measurements during the Migration of Dictyostelium Slugs Using Flexible Substrata, Biophys. J. 89, 3563–3576.

[13] Gardel, M. L., Sabass, B., Ji, L., Danuser, G., Schwarz, U. S., Waterman, C. M., (2008) Traction stress in focal adhesions correlates biphasically with actin retrograde flow speed, J. Cell Biol. 183(6), 999–1005.

[14] Stricker, J., Sabass, B., Schwarz, U. S., Gardel, M. L., (2010) Optimization of traction force microscopy for micron-sized focal adhesions, J. Phys.: Condens. Matter 22, 194104.

[15] Bridgman, P. C., Dave, S., Asnes, C. F., Tullio, A. N., Adelstein, R. S., (2001) Myosin IIB is required for growth cone motility, J Neurosci. 21(16), 6159–6169.

[16] Suter, D. M. and Forscher, P., (2001) Transmission of growth cone traction force through apCAM-cytoskeletal linkages is regulated by Src family tyrosine kinase activity, J. Cell Biol. 155(3), 427–438.

[17] Chan, C. E. and Odde, D. J., (2008) Traction dynamics of filopodia on compliant substrates, Science 322(5908), 1687–1691.

[18] Toriyama, M., Kozawa, S., Sakumura, Y., Inagaki, N., (2013) Conversion of a signal into forces for axon outgrowth through Pak1-mediated shootin1 phosphorylation, Curr. Biol. 23(6), 529–534.

[19] Wang, J. H. C. and Lin, J. S., (2007) Cell traction force and measurement methods, Biomechan. Model Mechanobiol., 6, 361–371.

[20] Landau, L. D. and Lifshitz, E. M., (1970) Theory of elasticity, In Course of Theoretical Physics, Vol. 7, 2nd Ed., Pergamon Press, Oxford, UK.

[21] Dembo, M., Oliver, T., Ishihara, A., Jacobson, K., (1996) Imaging the traction stresses exerted by locomoting cells with the elastic substratum method, Biophys. J. 70, 2008–2022.

[22] Dembo, M., and Wang, Y. L., (1999) Stresses at the cell-to-substrate interface during locomotion of fibroblasts, Biophys. J. 76, 2307–2316.

[23] Iwadate, Y., Yumura, S., (2008) Molecular dynamics and forces of a motile cell simultaneously visualized by TIRF and force microscopies, Biotechniques, 44(6), 739-750.

[24] Iwadate, Y., Yumura, S., (2008) Actin-based propulsive forces and myosin-II-based contractile forces in migrating Dictyostelium cells, J. Cell Science, 121, 1314-1324.

[25] Zienkiewicz, O. C., Morice, P. B, (1971), The finite element method in engineering science, London: McGraw-hill, 1977.

[26] Fournier, M. F., Sauser, R., Ambrosi, D., Meister, J. J., Verkhovsky, A. B., (2010) Force transmission in migrating cells, J. cell biology 188(2), 287-297.

[27] Ambrosi, D. (2006) Cellular traction as an inverse problem, SIAM Journal on Applied Mathematics, 66(6), 2049-2060.

[28] Butler, J. P., Tolic-Norrelykkex, I. M., Fabry, B., Fredberg, J. J., (2002) Traction fields, moments, and strain energy that cells exert on their surroundings, Am. J. Physiol. Cell Physiol. 282, C595–C605.

[29] Yang, Z., Lin, J. S., Chen, J., Wang, J. H., (2006) Determining substrate displacement and cell traction fields-a new approach, J. Theor. Biol. 242, 607–616.

[30] Schwarz, U. S., Balaban, N. Q., Riveline, D., Bershadsky, A., Geiger, B., Safran, S. A., (2002) Calculation of forces at focal adhesions from elastic substrate data: the effect of localized force and the need for regularization, Biophys. J. 83, 1380–1394.

[31] Sabass, B., Gardel, M. L., Waterman, C. M., Schwarz, U. S., (2008) High Resolution Traction Force Microscopy Based on Experimental and Computational Advances, Biophis. J. 94, 207–220.

[32] Forscher, P. and Smith, S. J., (1988) Actions of cytochalasins on the organization of actin filaments and microtubules in a neuronal growth cone, J. Cell Biol. 107, 1505–1516.

[33] Lin, C. H., Espreafico, E. M., Mooseker, M. S., Forscher, P., (1996) Myosin drives retrograde F-actin flow in neuronal growth cones, Neuron. 16, 769–782.

[34] Pollard, T. D. and Borisy, G. G., (2003) Cellular Motility Driven by Assembly and Disassembly of Actin Filaments, Cell, 112, 453–465.

[35] Pantaloni, D., Clainche, C. L., Carlier, M. F., (2001) Mechanism of actin-based motility, Science, 292, 1502–1506.

[36] Franck, C., Maskarinec, A. S., Tirrell, A. D., Ravichandran, G. (2011) Tree-Dimensional Traction Force Microscopy: A New Tool for Quantifying Cell-Matrix Interactions, PLos One, 6(3): e17833.

[37] Harris, K. A., Wild, P, Stopak, David., Silicone rubber substrata: a new wrinkle in the study of cell locomotion, Science, 208(4440), 177-179

[38] Horn, B. and Schunck, B., (1981) Determining optical flow, Artificial Intelligence, 17, 185-203.

[39] Brox, T., Bregler, C. and Malik, J., (2009) Large displacement optical flow, In CVPR.

[40] Tibshirani, R., (1996) Regression shrinkage and selection via the lasso, Journal of the Royal Statistical Society, Series B (Methodological), 267-288.

[41] Candes, E. and Tao, T., (2007) The Dantzig selector: Statistical estimation when p is much lager than n, Ann. Statist., 35(6), 2313-2351.

[42] Christophe, J, Marin, O., (2002) Extraction of spots in biological images using multiscale products, Pattern Recognition, 35(9), 1989-1996.

[43] Shimada, T., Toriyama, M., Uemura, K., Kamiguchi, H., Sugiura, T., Watanabe, N., and Inagaki, N. (2008). Shootin1 interacts with actin retrograde flow and L1-CAM to promote axon outgrowth. J. Cell Biol. 181, 817-829

[44] Toriyama, M., Shimada, T., Kim, K.B., Mitsuba, M., Nomura, E., Katsuta, K., Sakumura, Y., Roepstorff, P., and Inagaki, N. (2006). Shootin1: A protein involved in the organization of an asymmetric signal for neuronal polarization. J. Cell Biol. 175, 147-157

[45] Li, X., Gao, X., Liu, G., Xiong, W., Wu, J., and Rao, Y. (2008). Netrin signal transduction and the guanine nucleotide exchange factor DOCK180 in attractive signaling. Nat. Neurosci. 11, 28-35.

[46] Manser, E., Huang, H.Y., Loo, T.H., Chen, X.Q., Dong, J.M., Leung, T., and Lim, L. (1997). Expression of constitutively active alpha-PAK reveals effects of the kinase on actin and focal complexes. Mol. Cell Biol. 17, 1129-1143.

[47] Zhao, Z.S., Manser, E., Chen, X.Q., Chong, C., Leung, T., and Lim, L. (1998). A conserved negative regulatory region in alphaPAK: inhibition of PAK kinases reveals their morphological roles downstream of Cdc42 and Rac1. Mol. Cell Biol. 18, 2153-2163.

[48] Fukata, M., Kuroda, S., Nakagawa, M., Kawajiri, A., Itoh, N., Shoji, I., Matsuura, Y., Yonehara, S., Fujisawa, H., Kikuchi, A., et al. (1999). Cdc42 and Rac1 regulate the interaction of IQGAP1 with beta-catenin. J. Biol. Chem. 274, 26044-26050.

[49] Goto, H., and Inagaki, M. (2007). Production of a site- and phosphorylation state-specific antibody. Nat. Protoc. 2, 2574-2581.

[50] Woodcock, S.A., Jones, R.C., Edmondson, R.D., and Malliri, A. (2009). A modified tandem affinity purification technique identifies that 14-3-3 proteins interact with Tiam1, an interaction which controls Tiam1 stability. J. Proteome Res. 8, 5629-5641.

[51] Wang, Y.L., and Pelham, R.J., Jr. (1998). Preparation of a flexible, porous polyacrylamide substrate for mechanical studies of cultured cells. Methods Enzymol. 298, 489-496.

[52] Chan, C.E., and Odde, D.J. (2008). Traction dynamics of filopodia on compliant substrates. Science 322, 1687-1691.

[53] Bridgman, P.C., Dave, S., Asnes, C.F., Tullio, A.N., and Adelstein, R.S. (2001). Myosin IIB is required for growth cone motility. J. Neurosci. 21, 6159-6169.

[54] . Li, Y., Hu, Z., and Li, C. (1993). New method for measuring Poisson's ratio in polymer gels. J. Appl. Polym. Sci. 50, 1107-1111.

Appendix

A. Publication list

A.1 Journal paper

- Satoshi Kozawa, Yuichi Sakumura, Michinori Toriyama, Naoyuki Inagaki, Kazushi Ikeda, "Bayesian Cell Force Estimation Considering Force Directions", Neural Processing Letters, online published, Sep. 2013.

- Michinori Toriyama, Satoshi Kozawa, Yuichi Sakumura, Naoyuki Inagaki, "Conversion of a Signal into Forces for Axon Outgrowth through Pak1-Mediated Shootin1 Phosphorylation", Current Biology, Vol. 23, Issue 6, pp. 529-534, Mar. 2013.

A.2 International Conference

- Satoshi Kozawa, Yuichi Sakumura, Michinori Toriyama, Naoyuki Inagaki, Kazushi Ikeda, "An Estimation of Cell Forces with Hierarchical Bayes Approach Considering Cell Morphology", 19th International Conference, ICONIP 2012, Doha, Qatar, Nov. 2012

- Yusuke Kubo, Michinori Toriyama, Satoshi Kozawa, Kazushi Ikeda, Tadao Sugiura, Naoyuki Inagaki, "Cortactin functions as a clutch molecule to promote axon outgrowth", ASCB (The American Society for Cell Biology) 2012 Annual Meeting, San Francisco, CA, USA, Dec. 2012.